

## JGR Solid Earth

## RESEARCH ARTICLE

10.1029/2023JB028399

## Key Points:

- Frictional stability of glaucophane gouge is P-T dependent, with a change from  $v$ - $s$  to  $v$ - $w$  at  $\sim 300^\circ\text{C}$  with enhanced  $v$ - $w$  at lower stresses
- Minor  $v$ - $w$  of glaucophane gouge at critical stress conditions is favorable for slow slip events in subduction zones
- Frictional stability of glaucophane gouge upon fluid overpressures supports the observation of abundant intermediate-depth earthquakes

## Supporting Information:

Supporting Information may be found in the online version of this article.

## Correspondence to:

F. Zhang and Z.-Y. Yin,  
fengshou.zhang@tongji.edu.cn;  
zhenyu.yin@polyu.edu.hk

## Citation:

An, M., Zhang, F., Yin, Z.-Y., Huang, R., Elsworth, D., & Marone, C. (2024). Frictional strength and frictional instability of glaucophane gouges at blueschist temperatures support diverse modes of fault slip from slow slip events to moderate-sized earthquakes. *Journal of Geophysical Research: Solid Earth*, 129, e2023JB028399. <https://doi.org/10.1029/2023JB028399>

Received 7 DEC 2023

Accepted 24 SEP 2024

## Author Contributions:

**Conceptualization:** Mengke An, Derek Elsworth

**Data curation:** Mengke An

**Formal analysis:** Mengke An

**Methodology:** Mengke An

**Validation:** Rui Huang, Chris Marone


**Writing – original draft:** Mengke An

**Writing – review & editing:**

Fengshou Zhang, Zhen-Yu Yin,

Rui Huang, Derek Elsworth, Chris Marone

## Frictional Strength and Frictional Instability of Glaucophane Gouges at Blueschist Temperatures Support Diverse Modes of Fault Slip From Slow Slip Events to Moderate-Sized Earthquakes

Mengke An<sup>1,2</sup> , Fengshou Zhang<sup>3,4</sup> , Zhen-Yu Yin<sup>1</sup> , Rui Huang<sup>3,4</sup>, Derek Elsworth<sup>2,5</sup>, and Chris Marone<sup>5,6</sup> 

<sup>1</sup>Department of Civil and Environmental Engineering, The Hong Kong Polytechnic University, Kowloon, China,

<sup>2</sup>Department of Energy and Mineral Engineering, EMS Energy Institute and G3 Center, The Pennsylvania State University, University Park, PA, USA, <sup>3</sup>Department of Geotechnical Engineering, College of Civil Engineering, Tongji University, Shanghai, China, <sup>4</sup>Key Laboratory of Geotechnical & Underground Engineering of Ministry of Education, Tongji University, Shanghai, China, <sup>5</sup>Department of Geosciences, The Pennsylvania State University, University Park, PA, USA,

<sup>6</sup>Dipartimento di Scienze della Terra, La Sapienza Università di Roma, Rome, Italy

**Abstract** Fluid overpressure from the water released by subducted sediments and oceanic crust is an important mechanism for generating earthquakes via brittle failure and frictional instability. If unstable, such fault materials may also host diverse fault reactivation mechanisms from slow slip events to moderate-sized earthquakes in cold subduction zones. We examine this hypothesis for glaucophane gouge - a key index minerals for blueschist facies - at lower confining stresses where behavior is poorly understood. We measure friction and stability at temperatures of  $100^\circ\text{C}$ – $500^\circ\text{C}$  and effective normal stresses of 50–200 MPa, to explore the controls of temperature, stresses and excess pore fluid pressures on fault friction. The frictional coefficient of glaucophane at representative temperatures and stresses is  $\sim 0.70$ , insensitive to temperature but with a slight increase at lower effective stresses. Elevating temperature promotes a transition from velocity-strengthening to weak velocity-weakening behavior, indicating the destabilizing effect of high temperature downdip in subduction zones. Reducing effective normal stress or concomitantly elevating pore fluid pressure further strengthens the velocity-weakening response and would be manifest as moderate-sized earthquakes. Our results support the potential for enhanced unstable sliding of glaucophane gouges at lower effective stresses and blueschist facies temperatures - with weak to moderate velocity-weakening responses upon fluid pressurization vital for understanding the abundance of slow slip to moderate-sized earthquakes apparent in cold subduction zones.

**Plain Language Summary** Blueschist facies present in subduction zones with lower thermal gradient host abundant slow-slip and dynamic earthquakes—such events requiring critical stress conditions. Such blueschist layers are characterized by abundant fluids that are released as the slab descends and heats—resulting in large excess fluid pressures that may trigger slip on faults at depth. We measure the frictional properties of simulated faults containing glaucophane powders representative of these blueschist products at temperatures, stresses and especially fluid overpressures representative of the descending slab at the plate boundary. Results indicate a temperature-independent high frictional strength but a transition to unstable slip at both higher temperatures and increased fluid pressures. In the intermediate-depth subduction zone, depending on the fluid pressure, it is possible to generate earthquakes in a diverse range of modes such as slow-slip events through moderate-sized earthquakes. This can explain documented observations in this region. Our results highlight the importance of fluid pressurization and effective stress reduction in controlling such slow-slip and moderate-sized events at higher temperatures and for understanding earthquakes in subduction zones.

### 1. Introduction

Abundant intermediate-depth (moderate-sized) earthquakes observed in old and cold subduction zones, for example, offshore Hokkaido and Tohoku in northern Japan and Alaska in the United States, highlight the importance of fluid overpressures in inducing earthquakes under conditions prevalent in blueschist facies (Abers et al., 2013; Giuntoli et al., 2022; Hacker et al., 2003; Kim et al., 2015; Kita et al., 2006; Obara & Kato, 2016).

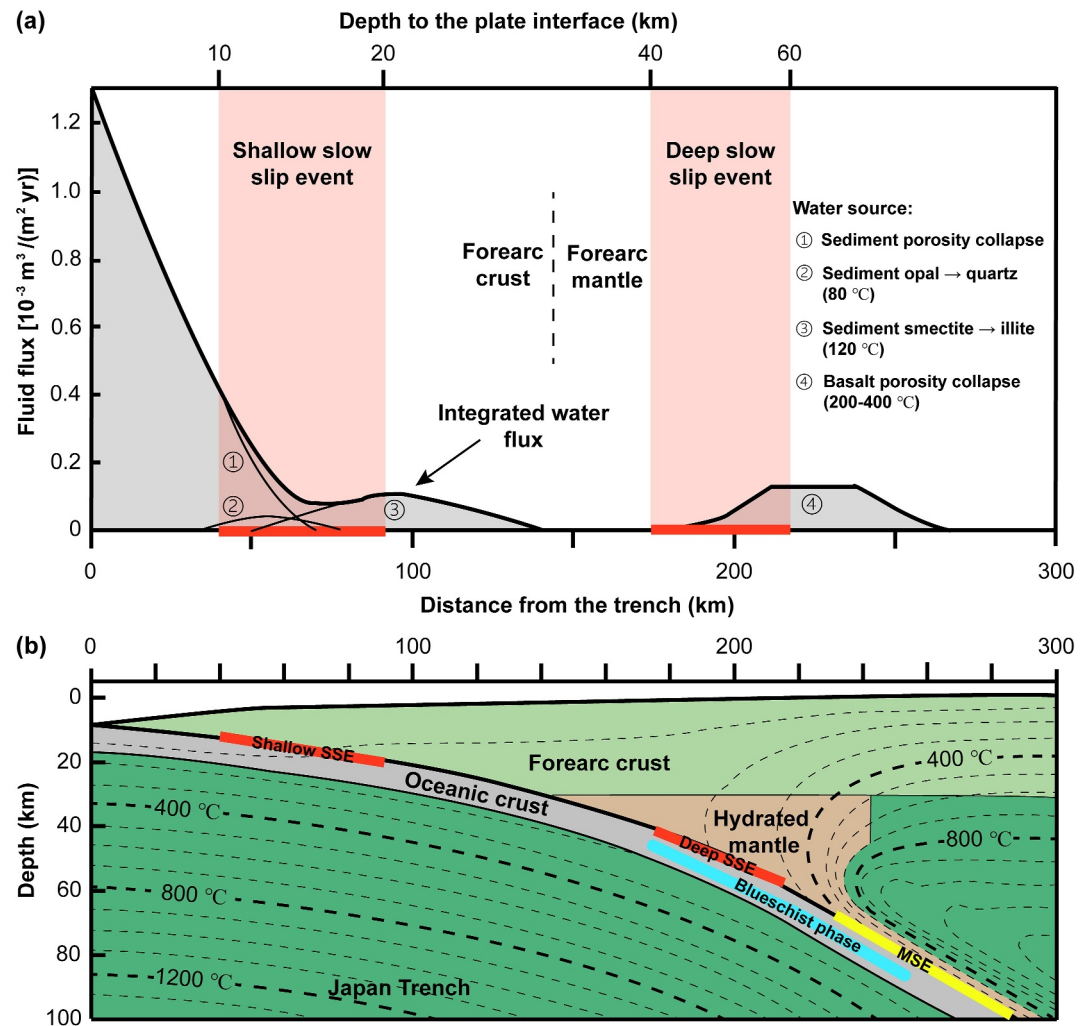


**Figure 1.** Schematic plot showing the fluid flux distribution and thermal structure along the Japan Trench. (a) Flux of water released from the subducted sediments and oceanic basalt crust estimated by Hyndman and Peacock (2003) with the locations of the possible shallow and deep slow slip regions (orange areas). (b) Thermal structure and temperature distribution along the Japan Trench (Peacock & Wang, 1999). Orange, yellow and cyan areas indicate the depth ranges for slow slip events (SSE), moderate-sized (MSE) earthquakes and the extent of the blueschist phase. Figure adapted from Hyndman and Peacock (2003), Gao and Wang (2017) and Nishikawa et al. (2023).

Meanwhile, regions hosting deep slow slip events are also characterized by abundant fluids and high pore fluid pressures, such as the Japan Trench (Kirkpatrick et al., 2021; Kodaira et al., 2004; Nishikawa et al., 2023; Ujiie et al., 2018) (Figure 1). Slow slip events and tectonic tremors (10–20 km depth) are also commonly linked with fluid overpressure from fluids released from sediment compaction, opal to quartz diagenetic transformation, and smectite to illite phase transformation (Hyndman & Peacock, 2003; Saffer & Tobin, 2011; Saffer & Wallace, 2015). Moreover, water supplied from pore collapse within basalts may be related to slow slip events within blueschist facies rocks (Nishikawa et al., 2023; Peacock & Wang, 1999; Uchida et al., 2016; Yokota & Koketsu, 2015) (Figure 1).

Excess fluids can increase fluid pressure and porosity while reducing effective stresses, which can cause embrittlement of the fault rocks (Kim et al., 2013; Ko et al., 1997; Miller et al., 2004; Murrell & Ismail, 1976; Scuderi & Collettini, 2016). Additionally, pore fluid overpressures may develop due to tectonic loading or compaction disequilibrium processes (e.g., thrusts from subduction forearcs and the accretionary wedge) if there is an impermeable seal or if the subducting fault zone is sufficiently thick and impermeable (Nishiyama et al., 2020; Saffer & Tobin, 2011; Tang et al., 2024). Moreover, fluid overpressures and low effective stresses

have been regarded as important prerequisites for the occurrence of shallow slow slip events (SSE), low frequency events (LFE) and episodic tremor and slip (ETS) when the faults exhibit frictional responses transitional from rate-strengthening to rate-weakening (Audet et al., 2009; Collettini et al., 2019; Kao et al., 2005; Kodaira et al., 2004; Saffer & Wallace, 2015). Thus, the related dependencies of strength and frictional stability on stress, fluid pressures and temperatures are important in understanding the controls of brittle failure on moderate-sized earthquakes and slow slip events in many settings.

Blueschist minerals are indicative of low temperature (<550°C) and high pressure (up to several GPa) metamorphism and are widely distributed in the Mesozoic and Cenozoic circum-Pacific and Alpine fold belts and oceanic plate subduction zones (Frisch et al., 2011; Maekawa et al., 1993; Stern, 2005). Glaucofanite and lawsonite are two key components of blueschist facies and are typically regarded as index minerals defining metamorphic grade (Carman & Gilbert, 1983; Jenkins & Corona, 2006; Maresch, 1977; Poli & Schmidt, 1995). Both minerals contain bound water in their crystal structures (~2.5 wt.% in glaucofanite and ~11.5 wt.% in lawsonite) but the breakdown of glaucofanite does not occur at depths above 240 km for a cold subduction geotherm (Peacock, 1993; Schmidt & Poli, 1994, 1998; Gao & Klemd, 2001; Hacker et al., 2003; Bang et al., 2021). Currently, lawsonite has been observed to produce fault stick-slip in lab experiments at high temperatures and very high pressures (of the order of GPa) (Okazaki & Hirth, 2016), although systematic observations of the frictional stability of glaucofanite-filled faults are limited. In addition, slow slip and episodic tremor have been reported in blueschist facies in subduction zones and linked to fluid overpressures from porosity collapse in basalt and within glaucofanite stability zone (Giuntoli et al., 2022; Kim et al., 2015; Muñoz-Montecinos et al., 2023; Nishikawa et al., 2023) (Figure 1). As a consequence, understanding the frictional properties of glaucofanite gouge under temperatures and stresses representative of cold subducting slabs is vital in constraining nucleation mechanisms of the spectrum of moderate-sized earthquakes, slow slip events (SSE) and episodic tremor and slip (ETS) present in subduction zones.

Existing study of mixed blueschist (glaucofanite-lawsonite) fault gouge materials demonstrate that fluid pressurization under hydrothermal conditions is a key mechanism contributing to frictional instability in glaucofanite-rich faults (Sawai et al., 2016). Although the frictional properties of blueschist assemblages are not necessarily represented by those of pure glaucofanite or lawsonite, these materials provide end-member responses for the friction and stability properties at relevant temperatures and pressures (e.g., Okamoto et al., 2020; Okazaki & Hirth, 2016). Additionally, as glaucofanite is one of the most important products in blueschist facies, understanding the friction and stability properties of pure glaucofanite gouge under hydrothermal conditions can help in defining the temperature and pressure conditions that promote the diverse modes of fault slip that are observed - from slow slip events to moderate-sized earthquakes.

Here, we present results of friction experiments on pure glaucofanite gouges under temperatures representative of blueschist facies (up to 500°C) and for varied effective stresses (50–200 MPa) and pore fluid pressures (30–80 MPa). Due to limitations of our apparatus, we only explore effective stresses up to 200 MPa and use these lower stress conditions to extrapolate trends in the control of effective stress on friction and stability. Although variations in effective normal stress in natural fault zones are primarily achieved through fluid over-pressure, we varied both the confining and pore fluid pressures in our experiments to independently deconvolve effects from both stresses and fluid pressures as representative of a variety of locations in the descending slab. Our observations highlight the importance of temperature and mineralogy on the diversity of habit of fault reactivation from slow slip events to moderate-sized earthquakes.

## 2. Experimental Methods

### 2.1. Gouge Preparation

We use glaucofanite (Figure 2a) collected from Baoding City, Hebei, northern China. After removing surface impurities, the glaucofanite was crushed and ground to particles <75 μm (Figure 2a). X-ray diffraction (XRD) results indicate that the glaucofanite powder was >99% pure with impurities primarily of calcite representing the remaining ~1 wt.% (Figure 2b). X-ray fluorescence spectrometry (XRF) indicates that the main components in the glaucofanite powders are SiO<sub>2</sub> (47.26% by weight), MgO (21.00%), Fe<sub>2</sub>O<sub>3</sub> (15.67%), Al<sub>2</sub>O<sub>3</sub> (10.74%), TiO<sub>2</sub> (1.56%), and Na<sub>2</sub>O (1.26%), with minor constituents of CaO (0.75%), P<sub>2</sub>O<sub>5</sub> (0.32%), Cr<sub>2</sub>O<sub>3</sub> (0.19%), NiO (0.11%), MnO (0.07%), V<sub>2</sub>O<sub>5</sub> (0.05%) and K<sub>2</sub>O (0.02%). Laser particle size analysis indicates a median particle size of the

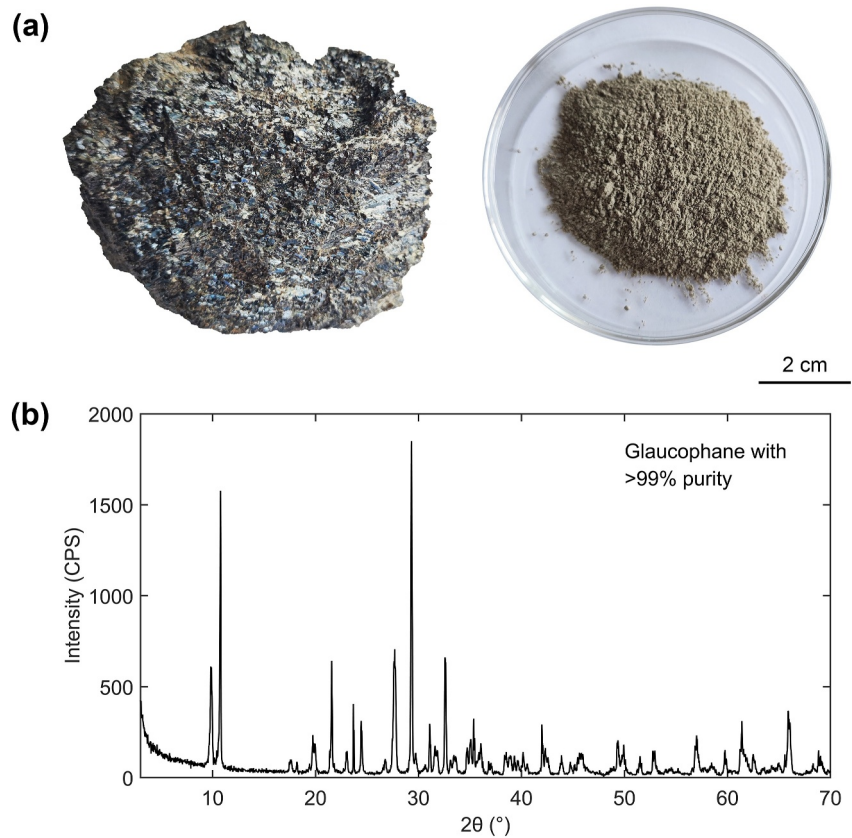


**Figure 2.** (a) Bulk glaucophane then crushed. (b) The X-ray diffraction (XRD) result for the glaucophane powder.

powders of 43.5  $\mu\text{m}$  with  $\sim 80$  vol.% of particles within the range 5.2–116  $\mu\text{m}$  (Figure S1 in Supporting Information S1).

## 2.2. Experimental Procedure

All experiments were completed using an argon gas-confined apparatus located at the Institute of Geology, China Earthquake Administration, Beijing, China (He et al., 2006). The apparatus comprises six components: (a) a fault gouge assembly system, (b) a pressure chamber that accommodates the sheared fault gouge, (c) an argon-gas pressurization system, (d) a pore-fluid pressurization system (e) a heating system (i.e., the heating furnace), and, (f) an electro-hydraulic servo-controlled loading system (Figure 3).

We used cylindrical samples with a 35° saw cut and gabbro driving blocks to impose shear on the glaucophane fault gouge. The gabbro driving blocks were 40 mm in height and 19.8 mm in diameter. For each test, the saw cut surfaces of the gabbro driving blocks were roughed by 200-mesh silicon carbide abrasive to anchor the fault gouge to the forcing blocks. Two holes (diameter of 2.5 mm) were drilled in the upper gabbro driving block for pore fluid access. Brass wire filters were inserted into these drill holes to inhibit gouge extrusion during shear and maintain the high-permeability of the fault system. We prepared glaucophane powders as a paste using deionized water and uniformly smeared them on the surface of the upper gabbro driving block. A leveling jig retained the gouge thickness to 1.0 mm before inserting into a 0.35 mm thick annealed copper jacket. High-hardness tungsten carbide and corundum blocks were placed above and below the gabbro and inside the copper jacket (Figure 3). The area between the furnace and the copper jacket was filled with boron nitride powder to minimize convection of the argon gas confining fluid—and ceramic wool was used to prevent leakage of the boron nitride powders. O-rings on steel end caps above and below the friction assembly sealed pore fluid pressure. The high-pressure seal on the upper piston prevents argon-gas leakage and provides the main seal for confining pressure. A Teflon sheet was placed between the lower steel end plug and the loading piston to eliminate frictional resistance and allow shear along that surface in concert with shear on the 35° saw cut. We used a two-zone heating system to maintain

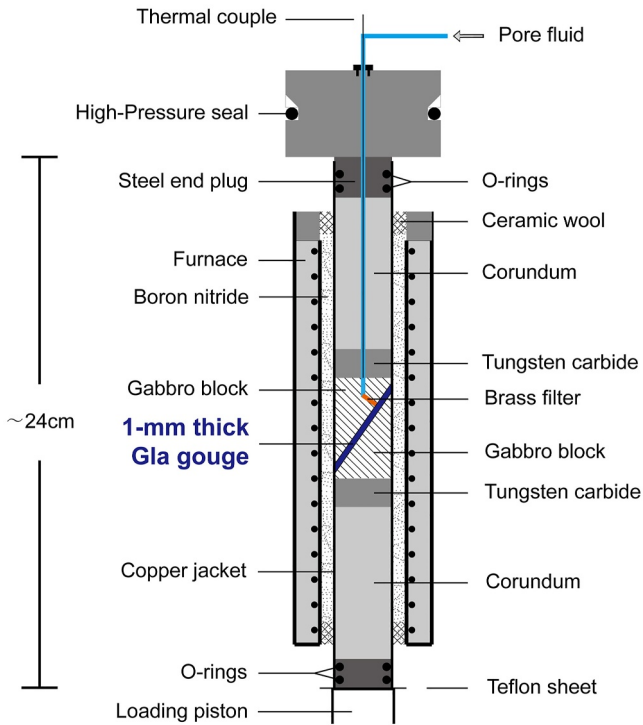


**Figure 3.** Schematic plot of the fault gouge and loading assembly for the triaxial shear apparatus. Gla = glaucophane.

uniform temperature on the fault zone and our measurements (see thermal couple in Figure 3) show maximum excursions of  $\pm 7^\circ\text{C}$  at  $\sim 600^\circ\text{C}$ . The maximum temperature in our experiments was  $500^\circ\text{C}$ . We used deionized water as the pore fluid for all experiments. As the duration of most experiments was less than  $\sim 10$  hr, the gabbro driving blocks would have negligible influence on either the fluid chemistry or gouge composition.

A total of eight shear experiments were completed at confining pressures of 55–130 MPa, pore fluid pressures of 30–80 MPa, temperatures of  $100^\circ\text{C}$ – $500^\circ\text{C}$ , and axial displacement rates of 0.04–1.0  $\mu\text{m/s}$  (Table 1). For our triaxial shear experiments, the relationship between the effective confining pressure ( $\sigma_{ceff}$ ) and effective normal stress ( $\sigma_{neff}$ ) is expressed by (Liu & He, 2020),

$$\sigma_{ceff} = \sigma_{neff}(1 - \mu \cdot \cot \alpha) \quad (1)$$

where  $\mu$  is the measured coefficient of friction and  $\alpha$  is the angle of the inclined fault driving block face relative to the loading axis. Thus, effective confining pressures of 25, 50 and 100 MPa correspond to effective normal stresses of  $\sim 50$ ,  $\sim 100$  and  $\sim 200$  MPa for the glaucophane gouge. Five shear tests: Gla-T100, Gla-T200, Gla-T300, Gla-T400 and Gla-T500 were performed at the same confining and pore fluid pressures ( $\sigma_c = 130$  MPa,  $P_f = 30$  MPa) but different temperatures ( $T = 100^\circ\text{C}$ – $500^\circ\text{C}$ ), to explore the effect of increasing temperature on the frictional and stability properties of the glaucophane gouge. Another three experiments Gla-T300 ( $\sigma_{neff} = 200$  MPa), Gla-T300-E100 ( $\sigma_{neff} = 100$  MPa) and Gla-T300-E50 ( $\sigma_{neff} = 50$  MPa) were completed at identical pore fluid pressures ( $P_f = 30$  MPa) and temperatures ( $T = 300^\circ\text{C}$ ) but different confining pressures ( $\sigma_c = 55$ –130 MPa), to investigate the effect of varied effective normal stress (decreased  $\sigma_c$ , constant  $P_f$ ) on gouge friction. A final experiment Gla-T300-P80 was performed to explore the effect of varied effective normal stress (Gla-T300-P80 and Gla-T300: elevated  $P_f$ , constant  $\sigma_c$ ) and of elevated pore pressure (Gla-T300-P80 and Gla-T300-E100: elevated  $P_f$ , constant  $\sigma_{neff}$ ) on gouge friction. We choose a temperature of  $300^\circ\text{C}$  to explore the effect of varied stresses on gouge frictional properties with this just below the super-critical temperature of the pore fluid above  $\sim 374^\circ\text{C}$  where the system is most stable.

As fluid pressures would increase with increasing temperatures, the confining and pore fluid pressures were first elevated to two-thirds of the desired values by the servo-controlled hydraulic ramp and pump, respectively. Subsequently, the temperature was elevated to the desired value by heating the furnace, followed by adjusting the confining and pore fluid pressures to the desired values. The confining and pore fluid pressures were controlled to  $\pm 0.3$  MPa and  $\pm 0.1$  MPa, respectively, during the entire experiment. Axial load, axial displacement and

**Table 1**  
Experiment Details

| Testing Id    | $\sigma_c$ (MPa) | $P_f$ (MPa) | $\sigma_{neff}$ (MPa) | $T$ ( $^\circ\text{C}$ ) | $V_a$ ( $\mu\text{m/s}$ )                      | $l_f$ (mm) | Velocity dependence |
|---------------|------------------|-------------|-----------------------|--------------------------|--|------------|---------------------|
| Gla-T100      | 130              | 30          | 200                   | 100                      | 1.0-0.2-0.04-0.2-1.0-0.2-0.04-0.2-1.0          | 3.98       | v-s                 |
| Gla-T200      | 130              | 30          | 200                   | 200                      | 1.0-0.2-0.04-0.2-1.0-0.2-0.04-0.2-1.0          | 3.96       | v-s                 |
| Gla-T300      | 130              | 30          | 200                   | 300                      | 1.0-0.2-0.04-0.2-1.0-0.2-0.04-0.2-1.0          | 3.97       | v-s, v-w            |
| Gla-T400      | 130              | 30          | 200                   | 400                      | 1.0-0.2-0.04-0.2-1.0-0.2-0.04-0.2-1.0          | 4.05       | v-s, v-w            |
| Gla-T500      | 130              | 30          | 200                   | 500                      | 1.0-0.2-0.04-0.2-1.0-0.2-0.04-0.2-1.0          | 3.98       | v-s, v-w            |
| Gla-T300-E100 | 80               | 30          | 100                   | 300                      | 1.0-0.2-0.04-0.2-1.0-0.2-0.04-0.2-1.0          | 3.97       | v-s, v-w            |
| Gla-T300-E50  | 55               | 30          | 50                    | 300                      | 1.0-0.2-0.04-0.2-1.0-0.2-0.04-0.2              | 2.90       | v-w                 |
| Gla-T300-P80  | 130              | 80          | 100                   | 300                      | 1.0-0.2-0.04-0.2-1.0-0.2-0.04-0.2-1.0-0.2-0.04 | 3.91       | v-s, v-w            |

Note. Symbols  $\sigma_c$ ,  $P_f$ ,  $\sigma_{neff}$ ,  $T$ ,  $V_a$ ,  $l_f$ , v-s, and v-w represent the confining pressure, pore fluid pressure, effective normal stress, temperature, axial velocity, final shear displacement, velocity-strengthening behavior and velocity-weakening behavior, respectively.



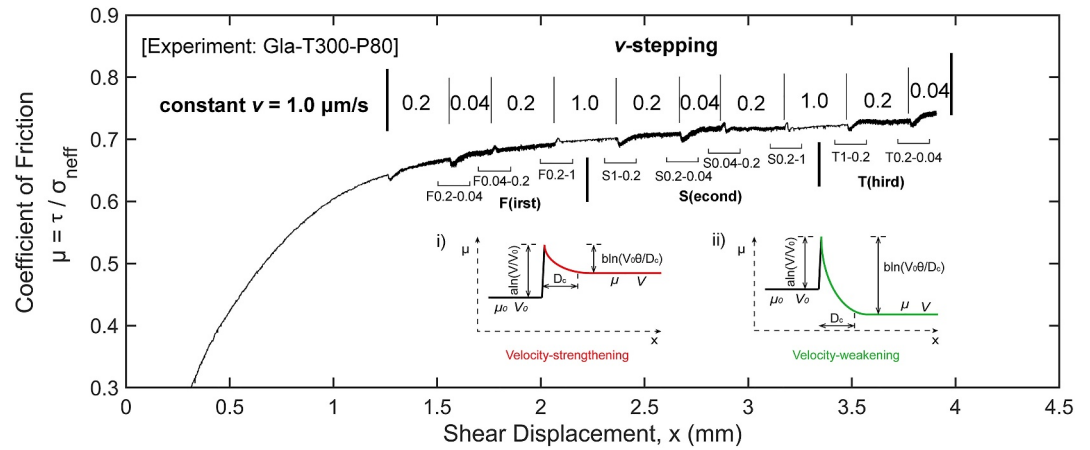


**Figure 4.** Typical experiment (Experiment: Gla-T300-P80) showing overall data trend and results of velocity step tests. Insets show the idealized responses of (i) velocity-strengthening and (ii) velocity-weakening behaviors, respectively. The boundaries showing the ranges for “First”, “Second” and “Third” sequences are marked.

temperature were respectively recorded by an internal high-precision load sensor, a displacement sensor and a temperature controller (Yamatate-Honeywell DCP30) at a sampling frequency of 1 Hz. The accuracy of the displacement sensor is  $\pm 0.01 \mu\text{m}$ . At the beginning of each shear test, the glaucophane gouge was sheared at an axial displacement rate of  $1.0 \mu\text{m/s}$  until slip hardening became muted. To evaluate the rate and state dependence of friction we performed velocity-step experiments using axial displacement rates of  $1.0\text{--}0.2\text{--}0.04\text{--}0.2\text{--}1.0 \mu\text{m/s}$ , equivalent to fault shear velocities of  $1.22\text{--}0.24\text{--}0.049\text{--}0.244\text{--}1.22 \mu\text{m/s}$  (Figure 4). For fault shear velocities of  $1.22$  and  $0.244 \mu\text{m/s}$  we imposed fault shear displacements of  $\sim 300 \mu\text{m}$  and this was reduced to  $\sim 200 \mu\text{m}$  for shear velocity of  $0.049 \mu\text{m/s}$ . The repeatability of experiments in this apparatus is indicated by previous work (He et al., 2006) and by systematic data trends for experiments at the same conditions (Table 1) with one parameter adjusted (temperature or confining pressure).

### 2.3. Data Analysis

Raw data of confining pressure ( $\sigma_c$ ), pore fluid pressure ( $P_f$ ), temperature ( $T$ ), axial stress ( $\sigma_a$ ) and axial displacement ( $l_a$ ) were recorded at a sampling rate of 1 Hz. We corrected for the change in frictional contact area with increasing axial displacement and stretching of the copper jacket. As the confining and pore fluid pressures remain constant only the axial stress is corrected for contact area. The corrected axial stress ( $\sigma_{ca}$ ) is expressed as,

$$\sigma_{ca} = \sigma_a / \left\{ 1 - \frac{2}{\pi} \left[ \arcsin \frac{\Delta l \tan \alpha}{2r} + \frac{\Delta l \tan \alpha}{2r} \sqrt{1 - \left( \frac{\Delta l \tan \alpha}{2r} \right)^2} \right] \right\} \quad (2)$$

where  $\Delta l$  and  $r$  represent the axial displacement and the radius of the forcing blocks, respectively. The shear resistance from the copper jacket was measured using smooth steel blocks with Teflon to eliminate friction (He et al., 2006).

After correcting the raw data, the coefficient of friction ( $\mu$ ) of the glaucophane gouge was calculated as the ratio of the shear stress ( $\tau$ ) and effective normal stress ( $\sigma_{neff}$ ), as,

$$\mu = \frac{\tau}{\sigma_{neff}} = \frac{\tau}{\sigma_n - P_f} \quad (3)$$

where  $\sigma_n$  denotes the applied normal stress. The calculated coefficients of friction in this study are actually the apparent coefficients of friction—referred-to here as coefficients of friction for simplicity. The velocity dependency of the glaucophane gouge was analyzed based on the rate- and state-friction (RSF) theory (Dieterich, 1979; Marone, 1998; Ruina, 1983) where the coefficient of friction ( $\mu$ ) is expressed as,

$$\mu = \mu_0 + a \ln\left(\frac{V}{V_0}\right) + b \ln\left(\frac{V_0\theta}{D_c}\right) \quad (4)$$

Here  $\mu$  is the instantaneous coefficient of friction at the current shear velocity  $V$  and state  $\theta$ ,  $\mu_0$  is the steady state coefficient of friction at the reference shear velocity  $V_0$ ,  $a$  and  $b$  are dimensionless parameters that describe the direct and evolutionary effects of friction upon a perturbation in velocity or  $\theta$ ,  $D_c$  represents the critical friction slip distance and  $\theta$  is a state variable that is best thought of as asperity contact age or fault gouge porosity. The evolution of the state variable ( $\theta$ ) with time can be described either by the Dieterich law (slowness law) (Dieterich, 1979) or the Ruina law (slip law) (Ruina, 1983), as,

$$\frac{d\theta}{dt} = 1 - \frac{V\theta}{D_c} \text{ (slowness law)} \quad (5)$$

$$\frac{d\theta}{dt} = -\frac{V\theta}{D_c} \ln\left(\frac{V\theta}{D_c}\right) \text{ (slip law)} \quad (6)$$

At steady state, the state variable  $\theta_{ss}$  ceases to evolve with time and thus  $d\theta/dt = 0$ , which means that  $\theta_{ss} = D_c/V$ . Using this value in Equation 4 shows that the rate dependent of steady state friction  $\mu_{ss}$  is:

$$a - b = \frac{\Delta\mu_{ss}}{\Delta \ln V} \quad (7)$$

where  $\Delta\mu_{ss}$  denotes the difference in steady state friction before and after a velocity step. The RSF parameters  $a$ ,  $b$ , and  $D_c$  are determined by accounting for finite stiffness of the loading machine and using an iterative least squares method (Reinen & Weeks, 1993). While the values of the friction rate parameter ( $a-b$ ) are independent of the state evolution law, we used both the Ruina and Dieterich laws to obtain values of the individual RSF parameters. Positive values of ( $a-b$ ) indicate velocity-strengthening whereby the steady state coefficient of friction increases with slip velocity ( $V > V_0$ ). Faults with positive ( $a-b$ ) would show only stable sliding and aseismic shear slip (Figure 4). Conversely, negative values of ( $a-b$ ) indicate velocity-weakening behavior (Figure 4) with a decrease in the steady state coefficient of friction with velocity ( $V > V_0$ ). Faults with negative ( $a-b$ ) exhibit potentially unstable sliding and seismic shear slip depending on the critical rheologic stiffness ( $K_{cr}$ ). Based on a simple spring-slider model and RSF theory, fault critical stiffness ( $K_{cr}$ ) is defined as (Rice & Ruina, 1983),

$$K_{cr} = \frac{(\sigma_n - P_f)(b - a)}{D_c} \quad (8)$$

where fault instability occurs only when the fault stiffness ( $K$ ) is smaller than the critical stiffness ( $K_{cr}$ ), that is,  $K < K_{cr}$  (Gu et al., 1984). A pre-requisite for slow-slip events is when the fault critical stiffness ( $K_{cr}$ ) approaches the fault stiffness ( $K$ ) (Scuderi et al., 2017), that is,  $K \approx K_{cr}$ .

#### 2.4. Microstructural Methods

At the conclusion of experiment, the cylindrical steel end plugs and corundum and tungsten carbide blocks were removed in sequence from the copper jacket, with the fault-driving-blocks remaining wrapped by the copper jacket. The fault driving blocks were then dried at 65°C for ~48 hr to remove any moisture inside the gouge zone. Subsequently, the fault driving blocks were placed in a cylindrical mold and vacuum saturated with epoxy resin. When the adhesive was hardened, the faults and driving blocks were sliced along the shear direction to obtain thin sections that were then polished, gold-coated and imaged by the scanning electron microscopy (SEM). The SEM images were collected on a Zeiss-Sigma SEM at an operating distance of 10.0 mm, a voltage of 20.00 kV, magnification factors of 200–250 and in backscattered electron mode. We focus on the gouge shear structures as defined by Logan et al. (1992) and particle size reductions in the moderately localized shear zones (MSZ) to strongly localized shear zones (SSZ). Strongly localized shear zones (SSZ) are characterized by >90% reduction in grain diameters to <10  $\mu\text{m}$ , while the remaining regions experiencing less comminution are defined as moderately localized shear zones (MSZ).

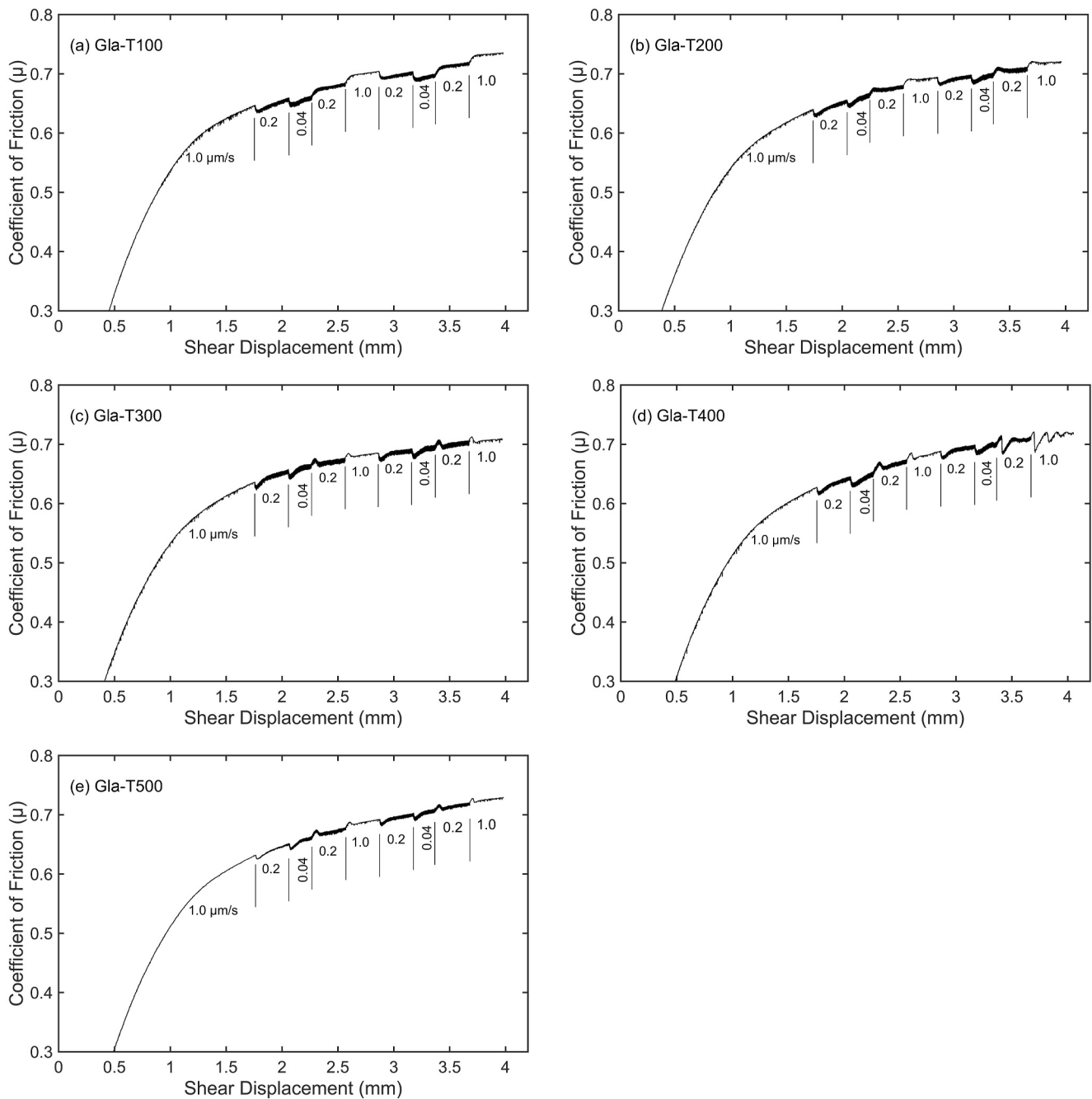


**Figure 5.** Coefficients of friction versus shear displacement for experiments at temperatures from 100°C (a) to 500°C (e). Velocity step test results are shown in each case.

### 3. Results—Friction/Stability Behavior and Microstructures

#### 3.1. Evolution of Friction and Stability With Temperature

The final shear displacements for tests at different temperatures all approach  $\sim 4.0$  mm (Table 1, Figure 5), with the final effective normal stresses of  $\sim 200$  MPa (Figure S2 in Supporting Information S1). The axial sliding velocities in each step are marked below the friction curves and the changes in friction with up- and down-steps in shear velocities are apparent from the curves (Figure 5). For the first 1 mm of shear displacement, all shear tests exhibit a linear increase in strength followed by in-elastic yield and strain-hardening with further shear. The gouge



**Table 2**  
Coefficient of Friction ( $\mu_{ss}$ ) and Friction Rate Parameter ( $a-b$ ) For all Experiments

| Testing Id    | $\mu_{ss}$ | $(a-b)$ values ( $\times 10^{-3}$ ) at different axial velocities ( $\mu\text{m/s}$ ) |           |        |        |           |           |        |        |           |
|---------------|------------|---|-----------|--------|--------|-----------|-----------|--------|--------|-----------|
|               |            | F0.2-0.04   | F0.04-0.2 | F0.2-1 | S1-0.2 | S0.2-0.04 | S0.04-0.2 | S0.2-1 | T1-0.2 | T0.2-0.04 |
| Gla-T100      | 0.701      | 4.3   | 8.4       | 8.9    | 7.7    | 7.1       | 8.7       | 7.9    | -      | -         |
| Gla-T200      | 0.691      | 1.6   | 3.2       | 5.5    | 3.5    | 3.9       | 3.1       | 5.7    | -      | -         |
| Gla-T300      | 0.682      | -2.1  | 1.6       | 2.7    | 0.6    | -1.2      | 0         | 0.7    | -      | -         |
| Gla-T400      | 0.682      | 1.0   | 3.0       | 0.7    | -0.4   | -1.5      | 0         | 1.6    | -      | -         |
| Gla-T500      | 0.688      | -1.4  | 1.7       | 2.9    | 0.6    | -1.7      | 1.3       | 1.9    | -      | -         |
| Gla-T300-E100 | 0.706      | -2.9  | 0.8       | 0.5    | -1.6   | -1.6      | -0.8      | -0.9   | -      | -         |
| Gla-T300-E50  | 0.753      | -5.0  | -1.1      | 0      | -3.3   | -3.1      | -1.2      | -      | -      | -         |
| Gla-T300-P80  | 0.716      | -4.7  | 0.5       | 1.3    | -3.5   | -4.9      | -0.7      | -1.6   | -4.0   | -6.5      |

*Note.* For most experiments, the coefficients of friction were evaluated at a set shear displacement of 2.75 mm and an axial velocity of 1.0  $\mu\text{m/s}$ , except for the tests Gla-T300-E50 and Gla-T300-P80 (both at an axial velocity of 0.04  $\mu\text{m/s}$ ). Test Gla-T300-E50 was terminated earlier than planned due to rupture of the copper jacket.

exhibits stable sliding in most cases up to 500°C, except for minor oscillatory slips at the final stage for test Gla-T400 (Figure 5d).

We report the coefficient of friction at a shear displacement of 2.75 mm and an axial sliding velocity of 1.0  $\mu\text{m/s}$  in Table 2 and as a function of temperature in Figure 6. Note that the coefficient of friction of glaucophane gouge is insensitive to temperature, with the values approaching 0.7 at all temperatures. Our results are broadly consistent with hornblende gouge at higher temperatures (Liu & He, 2020), but different from either the actinolite-rich (Okamoto et al., 2020) or glaucophane-rich (Sawai et al., 2016) gouges.

Values of the friction rate parameter ( $a-b$ ) were calculated following the methods described in Section 2.3 and reported in Table 2 and Figure 7. At temperatures  $\leq 300^\circ\text{C}$ , the frictional rate dependence is strongly influenced by temperature. Note that the transition from strong velocity-strengthening behavior ( $a-b = 0.0043$  to 0.0089) at  $T = 100^\circ\text{C}$ , to moderate velocity-strengthening behavior ( $a-b = 0.0016$  to 0.0057) at  $T = 200^\circ\text{C}$ , and then minor velocity-weakening behavior ( $a-b = -0.0021$  to 0.0027) at  $T = 300^\circ\text{C}$ . Conversely, at higher temperatures ( $T \geq 300^\circ\text{C}$ ), the friction rate dependence varies less with temperature. Note that values of ( $a-b$ ) range from  $-0.0015$  to 0.0030 at  $T = 400^\circ\text{C}$  and  $-0.0017$  to 0.0029 at  $T = 500^\circ\text{C}$ . Our results for frictional stability ( $a-b$ ) at different temperatures are also similar to those of hornblende (Liu & He, 2020).

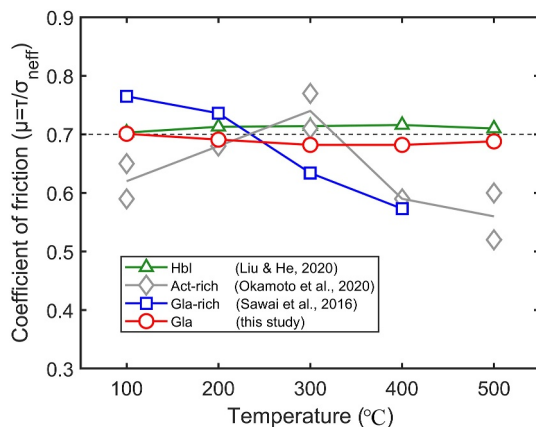


**Figure 6.** Coefficient of friction ( $\mu$ ) for the glaucophane gouge at temperatures of 100°C–500°C. Results for hornblende (Liu & He, 2020), actinolite-rich (Okamoto et al., 2020) and glaucophane-rich (Sawai et al., 2016) gouges are also displayed for comparison (Table S1 in Supporting Information S1).

The RSF parameters  $a$ ,  $b$ ,  $D_c$  and  $b/a$  were calculated using both the slowness and slip evolution laws as reported in Table 3 and Figures 8 and 9. The stiffness of our apparatus varies with temperature and we provide the stiffness values in Table 3. Both state evolution laws yield similar values of  $a$  and  $b$ , but small differences in  $D_c$  values, especially for the downward velocity steps. The  $D_c$  values calculated from the slowness evolution law (21–90  $\mu\text{m}$ ) are much larger than those calculated from the slip evolution law (21–59  $\mu\text{m}$ ) for the downward velocity steps (Figures 8e and 8f). Values of  $a$  and  $b$  in the upward velocity steps are higher than those for the downward velocity steps, while the  $D_c$  values exhibit the opposite trend, consistent with previous works showing differences between upsteps and downsteps (Rathbun & Marone, 2013). The responses of  $a$ ,  $b$  and  $b/a$  values to elevated temperature are broadly in accordance with the frictional rate parameter ( $a-b$ ) (Figure 7). According to Boatwright and Cocco (1996), weak seismic behavior is defined as frictional stability with  $(a-b) < 0$  and  $b/a-1 < 0.2$ . From Figure 9, values of  $b/a$  at temperatures of 100°C–500°C are primarily within the band 0.3–1.2, indicative of slight velocity-weakening behavior. In addition, values of the friction constitutive parameters  $a$  and  $b$  and friction rate parameter ( $a-b$ ) at the

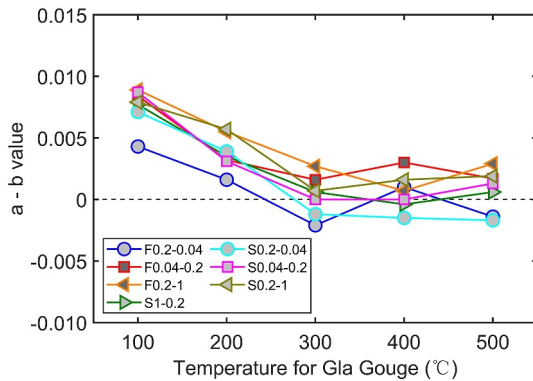


**Figure 7.** The friction rate parameter ( $a$ )–( $b$ ) as a function of temperature for glaucophane gouge. Legend shows axial velocities, with the symbols ‘F (irst)’ and ‘S (econd)’ indicating the sequence (see Figure 4).

(Table 2 and Figure 11a). However, elevating the pore fluid pressure from 30 ( $\mu = 0.71$ ) to 80 MPa ( $\mu = 0.72$ ) has little influence on the coefficient of friction (Table 2 and Figure 11a). At constant  $P_f = 30$  MPa, the range of the friction rate parameter ( $a$ – $b$ ) decreases from  $-0.0021$  to  $0.0027$  at  $\sigma_{neff} = 200$  MPa, to  $-0.0029$  to  $0.0008$  at  $\sigma_{neff} = 100$  MPa and  $-0.0050$  to  $0$  at  $\sigma_{neff} = 50$  MPa, indicating enhanced velocity-weakening at lower effective normal stresses (Figure 11b). At constant  $\sigma_c = 130$  MPa, the friction parameter ( $a$ – $b$ ) decreases from  $-0.0021$  to  $0.0027$  at  $P_f = 30$  MPa to  $-0.0065$  to  $0.0013$  at  $P_f = 80$  MPa, also indicating the destabilizing effect of lower effective normal stresses (Figure 11c). Similar observations of enhanced fault instability resulting from a decrease in effective stresses are reported not only in amphibole gouges (e.g., actinolite-rich and glaucophane-rich gouges, Okamoto et al., 2020; Sawai et al., 2016), but also in calcite-tremolite-talc mixed gouges (Niemeijer & Colletini, 2014) and epidote gouge (An et al., 2021). At constant  $\sigma_{neff} = 100$  MPa, the friction parameter ( $a$ – $b$ ) decreases from  $-0.0029$  to  $0.0008$  at  $P_f = 30$  MPa to  $-0.0065$  to  $0.0013$  at  $P_f = 80$  MPa, also demonstrating the destabilizing effect of higher pore fluid pressures (Figure 11d).

The RSF parameters  $a$ ,  $b$ , and  $D_c$  were calculated using both the slowness and slip evolution laws, with the results presented in Table 3 and Figures 12–14. Note that the parameters for the slowness and slip evolution laws are quite similar except for  $D_c$  and especially for down-stepped velocities. Values of  $a$  and  $b$  for up-steps are also higher than down-steps, with  $D_c$  values exhibiting the opposite trend. The responses of  $a$  and  $b$  values to the increase in effective normal stress are broadly consistent with frictional stability ( $a$ – $b$ ) (Figure 11b), while the response of  $b/a$  values show the opposite trend (Figure 13). In addition, values of  $b/a$  at lower effective normal stresses or higher pore fluid pressures are primarily within the range of 0.8–1.7 (Figures 13 and 14). The values of  $b/a$  in the velocity-weakening gouges of Figures 13 and 14 (within the range 1.0–1.7) are slightly higher than those in Figure 9 (within the range 1.0–1.2) and we classify these behaviors as moderate velocity-weakening. Similarly, the values of friction constitutive parameters  $a$  and  $b$  or frictional stability ( $a$ – $b$ ) are strongly affected by the history of the shear velocity but less by variations in shear displacement (Figure S5 in Supporting Information S1).

### 3.3. Evolution of Microstructures of Deformed Gouges

The microstructures observed in backscattered images of the deformed gouges at different temperatures and stresses are shown in Figures 15 and 16. At lower temperatures (100°C–200°C), the gouge returns to velocity-strengthening response with sparsely distributed localized shears (i.e.,  $R_1$  shears) and with Riedel shear angles within 10°–15° (Figures 15a and 15b). At higher temperatures (300°C–400°C), the gouge exhibits mild velocity-weakening and denser  $R_1$  localized shears, with Riedel shear angles increasing to 15°–20° (Figures 15c and 15d and Figure S3c in Supporting Information S1). However, at the highest temperature of 500°C, although the gouge shows minor velocity-weakening behavior, the  $R_1$  localized shears are also sparsely distributed, with Riedel shear angles reducing to  $\sim 10^\circ$ .

The comparisons between the moderately localized shear zones (MSZ) and strongly localized shear zones (SSZ) at  $T = 100$  and 300°C are shown in Figure S6 in Supporting Information S1. The glaucophane particles in the

same stress but different temperatures show a strong dependence on shearing velocity polarity as upsteps or downsteps, but are less affected by the incremental shear displacements (Figure S3 in Supporting Information S1).

### 3.2. Evolution of Friction and Stability With Effective Stresses

To explore the influence of effective stress on friction, we reduced the confining pressures from 130 to 55 MPa and elevated pore fluid pressures from 30 to 80 MPa (Figure S4 in Supporting Information S1). The final shear displacements in these tests were also  $\sim 4.0$  mm (Figure 10), except for test Gla-T300-E50 due to early rupture of the copper jacket (Figure 10b). The linear increase in friction at lower effective normal stresses occurs only at displacements in the range 0–0.5 mm. The gouge shows only stable sliding with no stick slips observed at the different effective stresses.

At  $T = 300^\circ\text{C}$ , the coefficients of friction increase from  $\sim 0.68$  at  $\sigma_{neff} = 200$  MPa, to  $\sim 0.71$  at  $\sigma_{neff} = 100$  MPa and  $\sim 0.75$  at  $\sigma_{neff} = 50$  MPa, indicating increased coefficients of friction at lower effective normal stresses

**Table 3**

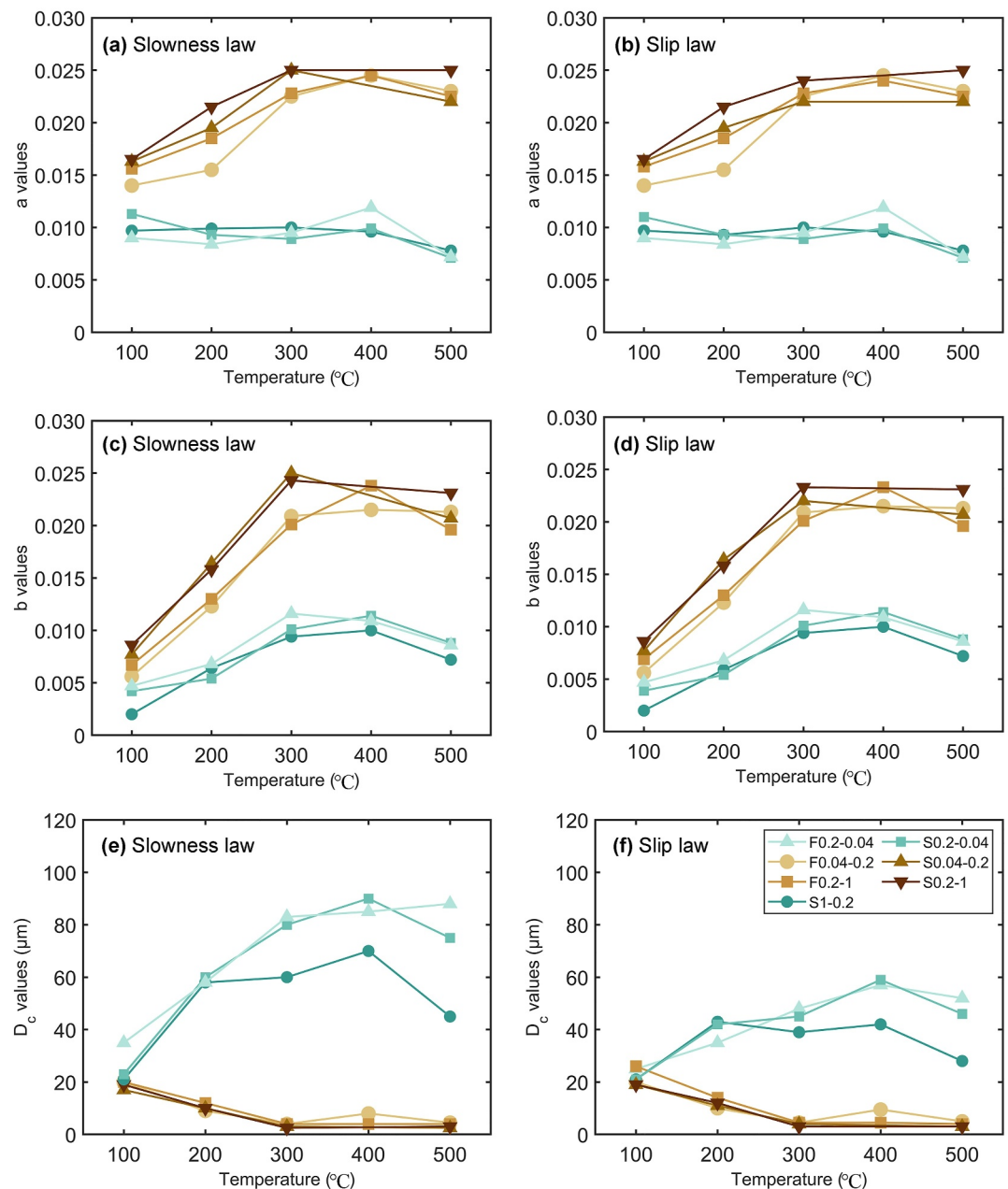
Experimental Results for the Frictional Constitutive Parameters  $a$ ,  $b$  and  $D_c$  Calculated by Both the Slowness and Slip Evolution Laws and the Normalized Fault Stiffness  $k$

| Testing Id    | Friction law | $a$ values ( $\times 10^{-3}$ ) at different axial velocities ( $\mu\text{m/s}$ ) |           |        |        |           |           |        |        |           |           | $b$ values ( $\times 10^{-3}$ ) at different axial velocities ( $\mu\text{m/s}$ ) |        |        |           |           |        |        |           |
|---------------|--------------|---|-----------|--------|--------|-----------|-----------|--------|--------|-----------|-----------|---|--------|--------|-----------|-----------|--------|--------|-----------|
|               |              | F0.2-0.04   | F0.04-0.2 | F0.2-1 | S1-0.2 | S0.2-0.04 | S0.04-0.2 | S0.2-1 | T1-0.2 | T0.2-0.04 | F0.2-0.04 | F0.04-0.2   | F0.2-1 | S1-0.2 | S0.2-0.04 | S0.04-0.2 | S0.2-1 | T1-0.2 | T0.2-0.04 |
| Gla-T100      | Slowness     | 9.0   | 14.0      | 15.6   | 9.7    | 11.3      | 16.4      | 16.5   | -      | -         | 4.7       | 5.6   | 6.7    | 2.0    | 4.2       | 7.7       | 8.6    | -      | -         |
|               | Slip         | 9.0   | 14.0      | 15.8   | 9.7    | 11.0      | 16.4      | 16.5   | -      | -         | 4.7       | 5.6   | 6.9    | 2.0    | 3.9       | 7.7       | 8.6    | -      | -         |
| Gla-T200      | Slowness     | 8.4   | 15.5      | 18.5   | 9.9    | 9.3       | 19.5      | 21.5   | -      | -         | 6.8       | 12.3  | 13.0   | 6.4    | 5.4       | 16.4      | 15.8   | -      | -         |
|               | Slip         | 8.4   | 15.5      | 18.5   | 9.4    | 9.3       | 19.5      | 21.5   | -      | -         | 6.8       | 12.3  | 13.0   | 5.9    | 5.4       | 16.4      | 15.8   | -      | -         |
| Gla-T300      | Slowness     | 9.5   | 22.5      | 22.8   | 10.0   | 8.9       | 25.0      | 25.0   | -      | -         | 11.6      | 20.9  | 20.1   | 9.4    | 10.1      | 25.0      | 24.3   | -      | -         |
|               | Slip         | 9.5   | 22.5      | 22.8   | 10.0   | 8.9       | 22.0      | 24.0   | -      | -         | 11.6      | 20.9  | 20.1   | 9.4    | 10.1      | 22.0      | 23.3   | -      | -         |
| Gla-T400      | Slowness     | 11.9  | 24.5      | 24.5   | 9.6    | 9.9       | -         | -      | -      | -         | 10.9      | 21.5  | 23.8   | 10.0   | 11.4      | -         | -      | -      | -         |
|               | Slip         | 11.9  | 24.5      | 24.0   | 9.6    | 9.9       | -         | -      | -      | -         | 10.9      | 21.5  | 23.3   | 10.0   | 11.4      | -         | -      | -      | -         |
| Gla-T500      | Slowness     | 7.2   | 23.0      | 22.5   | 7.8    | 7.1       | 22.0      | 25.0   | -      | -         | 8.6       | 21.3  | 19.6   | 7.2    | 8.8       | 20.7      | 23.1   | -      | -         |
|               | Slip         | 7.2   | 23.0      | 22.5   | 7.8    | 7.1       | 22.0      | 25.0   | -      | -         | 8.6       | 21.3  | 19.6   | 7.2    | 8.8       | 20.7      | 23.1   | -      | -         |
| Gla-T300-E100 | Slowness     | 7.7   | 22.8      | 23.8   | 8.0    | 8.2       | 20.8      | 20.8   | -      | -         | 10.6      | 22.0  | 23.3   | 9.6    | 9.8       | 21.6      | 21.7   | -      | -         |
|               | Slip         | 7.7   | 22.8      | 23.8   | 7.4    | 8.2       | 20.8      | 20.8   | -      | -         | 10.6      | 22.0  | 23.3   | 9.0    | 9.8       | 21.6      | 21.7   | -      | -         |
| Gla-T300-E50  | Slowness     | 7.3   | 18.9      | 19.1   | 7.8    | 7.8       | 18.4      | -      | -      | -         | 12.3      | 20.0  | 19.1   | 11.1   | 10.9      | 19.6      | -      | -      | -         |
|               | Slip         | 7.3   | 18.9      | 19.1   | 7.8    | 7.8       | 18.4      | -      | -      | -         | 12.3      | 20.0  | 19.1   | 11.1   | 10.9      | 19.6      | -      | -      | -         |
| Gla-T300-P80  | Slowness     | 9.3   | 23.3      | 23.3   | 9.5    | 9.5       | 20.3      | 19.8   | 9.0    | 8.5       | 14.0      | 22.8  | 22.0   | 13.0   | 14.4      | 21.0      | 21.4   | 13.0   | 15.0      |
|               | Slip         | 9.3   | 23.3      | 23.3   | 9.5    | 9.5       | 20.3      | 19.8   | 9.0    | 8.5       | 14.0      | 22.8  | 22.0   | 13.0   | 14.4      | 21.0      | 21.4   | 13.0   | 15.0      |

| Testing Id    | Friction law | $D_c$ values ( $\mu\text{m}$ ) at different axial velocities ( $\mu\text{m/s}$ ) |           |        |        |           |           |        |        |           |       | Normalized fault stiffness $k$ (mm) |
|---------------|--------------|--|-----------|--------|--------|-----------|-----------|--------|--------|-----------|-------|-------------------------------------|
|               |              | F0.2-0.04  | F0.04-0.2 | F0.2-1 | S1-0.2 | S0.2-0.04 | S0.04-0.2 | S0.2-1 | T1-0.2 | T0.2-0.04 |       |                                     |
| Gla-T100      | Slowness     | 35   | 20        | 20     | 21     | 23        | 17        | 19     | -      | -         | 0.542 |                                     |
|               | Slip         | 25   | 20        | 26     | 21     | 21        | 19        | 19     | -      | -         |       |                                     |
| Gla-T200      | Slowness     | 58   | 9         | 12     | 58     | 60        | 10        | 10     | -      | -         | 0.500 |                                     |
|               | Slip         | 35   | 10        | 14     | 43     | 42        | 11        | 12     | -      | -         |       |                                     |
| Gla-T300      | Slowness     | 83   | 4         | 4      | 60     | 80        | 3         | 2.5    | -      | -         | 0.499 |                                     |
|               | Slip         | 48   | 4.5       | 4.5    | 39     | 45        | 4         | 3      | -      | -         |       |                                     |
| Gla-T400      | Slowness     | 85   | 8         | 4      | 70     | 90        | -         | -      | -      | -         | 0.506 |                                     |
|               | Slip         | 57   | 9.5       | 4.5    | 42     | 59        | -         | -      | -      | -         |       |                                     |
| Gla-T500      | Slowness     | 88   | 4.5       | 4      | 45     | 75        | 2.5       | 3      | -      | -         | 0.501 |                                     |
|               | Slip         | 52   | 5         | 4      | 28     | 46        | 3         | 3      | -      | -         |       |                                     |
| Gla-T300-E100 | Slowness     | 49   | 1.5       | 1.3    | 62     | 67        | 2.5       | 1.4    | -      | -         | 0.561 |                                     |
|               | Slip         | 32   | 1.7       | 1.4    | 42     | 39        | 2.8       | 1.7    | -      | -         |       |                                     |
| Gla-T300-E50  | Slowness     | 57   | 1.7       | 1.2    | 59     | 43        | 1.0       | -      | -      | -         | 0.758 |                                     |
|               | Slip         | 34   | 1.8       | 1.2    | 36     | 26        | 1.0       | -      | -      | -         |       |                                     |
| Gla-T300-P80  | Slowness     | 67   | 1.1       | 1.4    | 66     | 74        | 1.4       | 1.6    | 42     | 60        | 0.729 |                                     |
|               | Slip         | 37   | 1.2       | 1.6    | 42     | 44        | 1.5       | 1.6    | 25     | 34        |       |                                     |

MSZ tend to be  $> 50 \mu\text{m}$ , while the particles in the SSZ are smaller,  $< 10 \mu\text{m}$  (Figures S3a-S3b in Supporting Information S1). We also estimate the proportions of the moderately localized shear zones (MSZ) with larger particles (yellow percentages areas in Figure 17) to the strongly localized shear zones with very fine particles (gray percentages in Figure 17). Results show that temperature has a negligible influence on the proportions of MSZ and SSZ for  $T \leq 400^\circ\text{C}$ . However, when the temperature is increased to  $500^\circ\text{C}$ , the proportion of the



**Figure 8.** Friction constitutive parameters  $a$ ,  $b$ , and  $D_c$  at temperatures of 100°C–500°C, (a)  $a$  values, calculated using the slowness evolution law, (b)  $a$  values, calculated using the slip evolution law, (c)  $b$  values, calculated using the slowness evolution law, (d)  $b$  values, calculated using the slip evolution law, (e)  $D_c$  values, calculated using the slowness evolution law, and (f)  $D_c$  values, calculated using the slip evolution law.

moderate shear zones has increased by  $\sim 10\%$ . The reduction in the proportion of SSZ for test Gla-T500 may be due to more ductile deformation at this high temperature where the gouge particles undergo less crushing (Zhang & He, 2016).

From Figure 16, the characteristics of the shear bands in the deformed gouge significantly differ at varied stress conditions. At  $T = 300^\circ\text{C}$ , with a decrease in the effective normal stress, the deformed shear bands exhibit a transition from dense  $R_1$  localized shears at  $\sigma_{\text{neff}} = 200$  MPa (Figure 15c), to sparse localized shears at  $\sigma_{\text{neff}} = 100$  MPa (Figures 16a and 16b) and mostly moderate shear zones and boundary shears (B shears) at  $\sigma_{\text{neff}} = 50$  MPa (Figure 16c and Figure S3d in Supporting Information S1). Meanwhile, the moderate shear zones

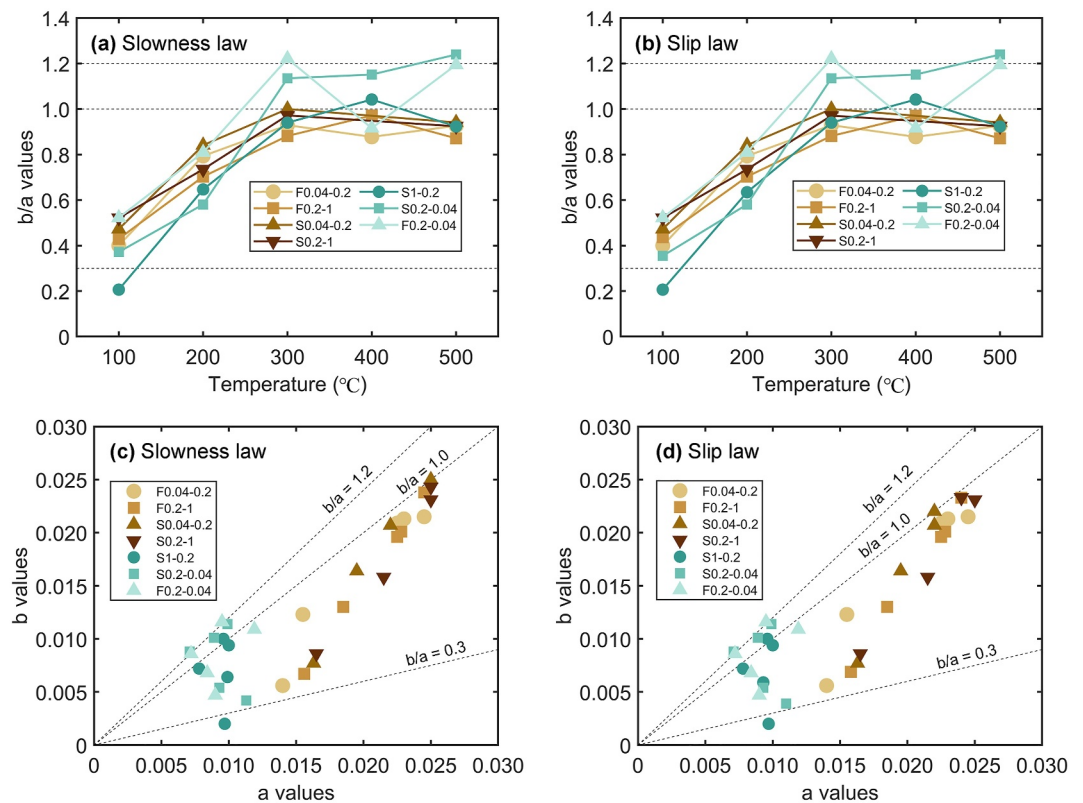


**Figure 9.** Frictional constitutive parameter  $b/a$  and  $b$  values versus  $a$  values at temperatures of 100°C–500°C. (a)  $b/a$  values, calculated using the slowness evolution law, (b)  $b/a$  values, calculated using the slip evolution law, (c)  $b$  values versus  $a$  values, calculated using the slowness evolution law, (d)  $b$  values versus  $a$  values, calculated using the slip evolution law.

(MSZ) account for the half of the gouge shear bands by proportion at  $\sigma_{neff} = 200$  MPa, but increase to three quarters at  $\sigma_{neff} = 100$  MPa and near the full proportion at the lowest effective normal stress of 50 MPa (Figure 17).

## 4. Discussion

### 4.1. Weak to Moderate Velocity-Weakening Response of Glaucophane Gouge

The friction rate parameter ( $a-b$ ) is not only a key parameter to assess fault frictional stability and differentiate between sliding behaviors, but also an important characteristic in exploring fault nucleation processes (Ampuero & Rubin, 2008; Mikumo, 1992). The glaucophane gouge exhibits velocity-weakening behavior at  $\sigma_c = 130$  MPa,  $P_f = 30$  MPa and temperatures of 300°C–500°C (Figure 7), with ( $b-a$ ) values within the range 0–0.0021 and ratios of  $b/a$  primarily within 1.0–1.2 (Figure 9). These all indicate weak velocity-weakening response (frictional stability ( $a-b$ ) < 0 and  $b/a-1$  < 0.2) and potentially seismic behavior for the tested glaucophane gouge at higher temperatures (e.g., Boatwright & Cocco, 1996). Moreover, the values of ( $b-a$ ) for glaucophane gouge are also an indicator of the likelihood of slow-slip events (SSE) and episodic tremor and slip (ETS) (Liu & He, 2020). Lowering the effective normal stresses or elevating the pore fluid pressures all further destabilize the glaucophane gouge (Figure 11). The ( $b-a$ ) values and ratios of  $b/a$  at lower stresses increase to 0–0.0065 and 1.0–1.7 (Figures 13 and 14), respectively, indicating a moderate velocity-weakening response.

Compared with the frictional stability of glaucophane-rich gouge in Sawai et al. (2016), the actinolite-rich gouge in Okamoto et al. (2020), or the amphibolite gouge in Fagereng and Ikari (2020), they show higher ( $b-a$ ) values at both room and high temperatures. Sawai et al. (2016) initially explored the frictional stability of glaucophane-rich gouge (glaucophane:lawsonite at 66:23) at  $\sigma_{neff} = 25$ –200 MPa,  $P_f = 25$ –200 MPa,  $T = 23$ °C–400°C and shear velocities of 0.1–100  $\mu\text{m/s}$  via ring shear. They report velocity-weakening responses at temperatures of 200°C–400°C with ( $b-a$ ) values of 0–0.02 and enhanced frictional stability at higher effective normal stresses. Although



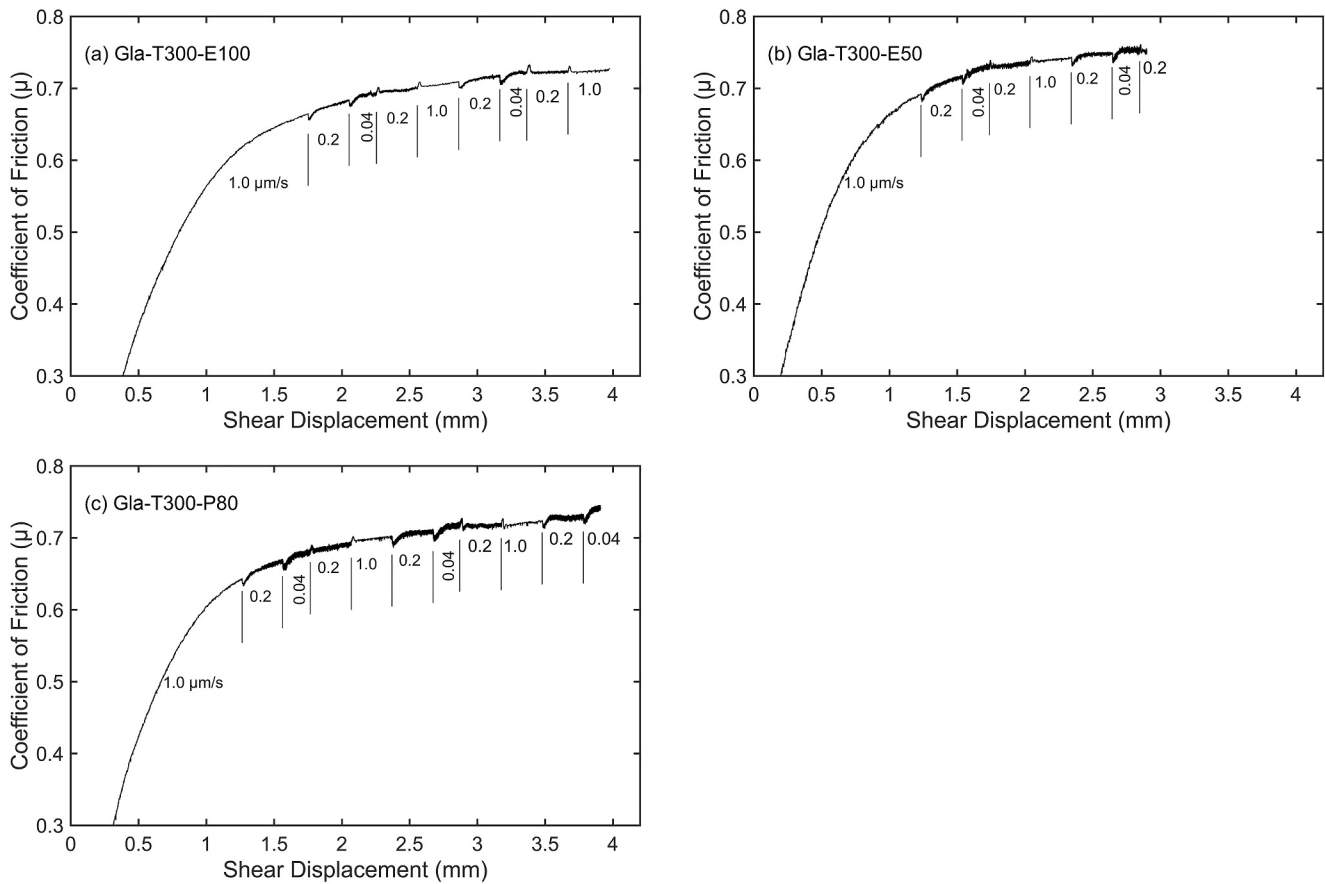


**Figure 10.** Coefficient of friction ( $\mu$ ) versus shear displacement for different effective stresses, (a) Gla-T300-E100, (b) Gla-T300-E50, and (c) Gla-T300-P80.

the mineral composition in our tested glaucophane gouge is different from the glaucophane-rich gouge of Sawai et al. (2016), the temperatures to promote velocity-weakening are broadly consistent with Sawai et al. (2016), and both experimental results show enhanced frictional instability at lower effective normal stresses. Okamoto et al. (2020) conducted ring shear experiments on actinolite-chlorite (85:15) mixtures at conditions of  $\sigma_{neff} = 50\text{--}200$  MPa,  $P_f = 50\text{--}200$  MPa,  $T = 23^\circ\text{C}\text{--}600^\circ\text{C}$  and shear velocities of  $0.3\text{--}100$   $\mu\text{m/s}$ . The results indicate velocity-weakening behaviors at  $\sigma_{neff} = P_f = 50$  MPa,  $T = 300^\circ\text{C}\text{--}400^\circ\text{C}$  and shear velocities of  $0.3\text{--}3$   $\mu\text{m/s}$ , with  $(b-a)$  values ranging from 0.002 to 0.011. Fagereng and Ikari (2020) performed direct shear tests on amphibolite gouge (89% hornblende, with minor quartz, feldspar and phlogopite) at room temperature,  $\sigma_n = 10$  MPa, shear velocities of  $0.1\text{--}30$   $\mu\text{m/s}$  and water-saturated conditions. The results show velocity-weakening response even at room temperature, with values of  $(b-a)$  ranging from 0 to 0.02. The discrepancies in values of  $(b-a)$  may derive from the different testing conditions and degrees of shear localization, including different net shear strains, confining stresses and shear velocities. Consistent among them, however, was fault instability promoted by fluid pressurization or lower effective stresses (Okamoto et al., 2020; Sawai et al., 2016). Our results also show a transition from weak to moderate velocity-weakening response due to an increase in pore fluid pressures or reduction in effective normal stresses (Figure 11). Additionally, the ranges of  $(a-b)$  and  $b/a$  obtained from the experiments are consistent with the slip modes that range from slow slip events (SSE) to dynamic earthquakes depending on the fault stiffness, critical stiffness, effective normal stress and  $D_c$  values.

The difference in frictional stability  $(a-b)$  between the cases for velocity upsteps and downsteps is less than  $\sim 0.05$  as indicated by Figures 7 and 11b - however, values of  $a$  and  $b$  may differ by  $\sim 0.015$  (e.g., Figure 8a). Asymmetry between upsteps and downsteps is anticipated by the Dieterich/Ruina evolution laws because in one case state evolution is dictated by time (Dieterich law) and in the other (Ruina) by slip. Notably, this effect is muted in both  $(a-b)$  and  $a/b$ , since the increase in the direct effect ( $a$ ) is directly compensated by an equivalent increase in the evolutionary effect ( $b$ ). We speculate that the higher upstep magnitudes of  $a$  and  $b$  result from chemically

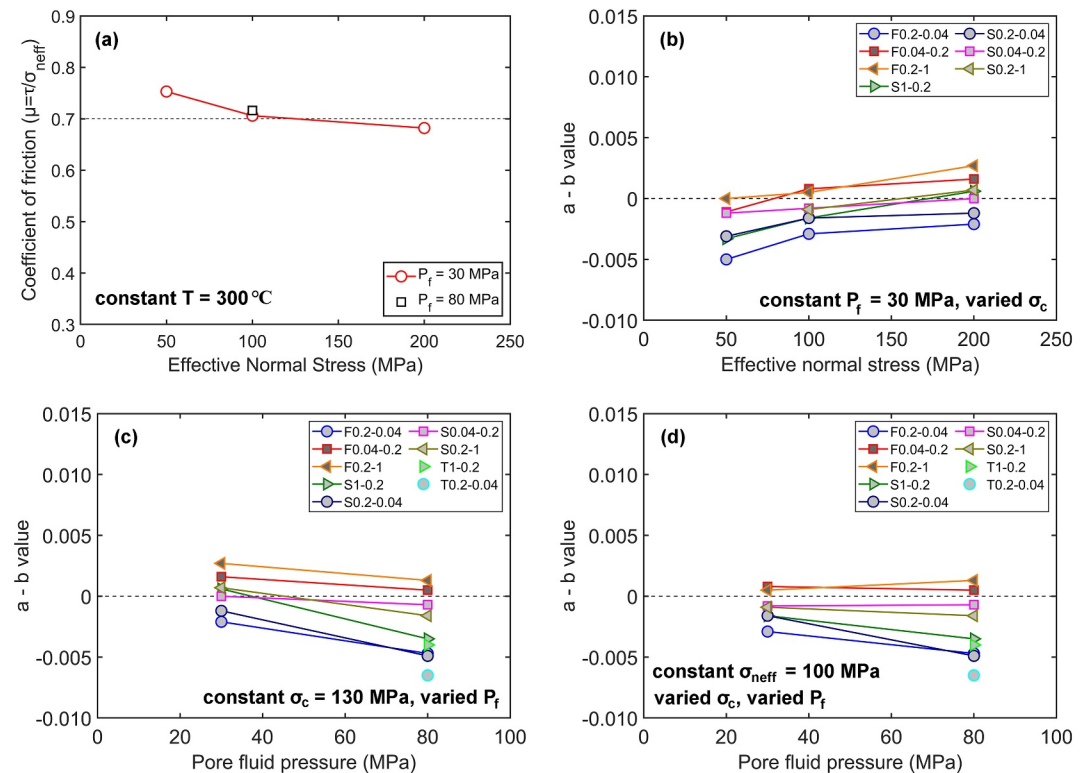


**Figure 11.** (a) Coefficient of friction ( $\mu$ ) at varied normal stresses and constant  $T = 300^\circ\text{C}$ . Results for frictional stability (a)–(b) at (b) a constant  $P_f = 30$  MPa, but different confining pressures, (c) a constant  $\sigma_c = 130$  MPa, but different pore fluid pressures, and (d) a constant  $\sigma_{\text{neff}} = 100$  MPa, but different confining and pore fluid pressures.

mediated strengthening, for example, by pressure solution increasing grain-grain contact areas that are then lost post-peak strength. This pressure solution effect will be greater as loading builds (upsteps), compared to that in de-stressing (downstep). The observation that  $D_c$  also systematically reduces in upsteps suggests that the effect is real—rather than, for example, a loading/unloading hysteresis in the load cell—since the effect is manifest in an independent measuring system for displacement. Additionally, the asymmetry of RSF friction parameters in granular fault gouges could also be interpreted using the model proposed by Marone et al. (2009) and Rathbun and Marone (2013). In this, dilation driven by shear stress and grain rearrangement plays an important role in the shear behavior of granular gouge. The key reason for the asymmetry is that the granular dilation requires shear strain and interparticle slip, but compaction may occur with only a change in stress.

#### 4.2. Dependence of Glaucophane Gouge Stability on Temperature and Effective Stress

The current experiments on the glaucophane gouge at  $\sigma_c = 130$  MPa,  $P_f = 30$  MPa and  $T = 100^\circ\text{C}$ – $500^\circ\text{C}$  exhibit two different fault sliding behaviors. These are the velocity-strengthening response ( $a-b > 0$ ) at  $T = 100^\circ\text{C}$ – $200^\circ\text{C}$ , and the weak velocity-weakening response ( $a-b < 0$ ) at  $T = 300^\circ\text{C}$ – $500^\circ\text{C}$  (Figure 7). The critical temperature for transition from velocity-strengthening to velocity-weakening behavior may coincidentally be the same as that for the hornblende and actinolite-rich gouges (Liu & He, 2020; Okamoto et al., 2020) - but it should be noted that the testing conditions of these experiments are different. Although the highest temperature in our experiments reaches  $500^\circ\text{C}$ , we can only observe the first frictional stability transition at this temperature range and the second stability transition from velocity-weakening to velocity-strengthening may occur at a much higher temperature (King & Marone, 2012; Liu & He, 2020). However, according to the temperature-pressure relationship for different metamorphic phases (Frisch et al., 2011), glaucophane is primarily present at temperatures below  $500^\circ\text{C}$  and thus we did not further elevate the testing temperature.

Likely mechanisms controlling the change in ( $a-b$ ) with temperature for the glaucophane gouge can be partially illuminated by using the microphysical models proposed by Niemeijer and Spiers (2007) and den Hartog

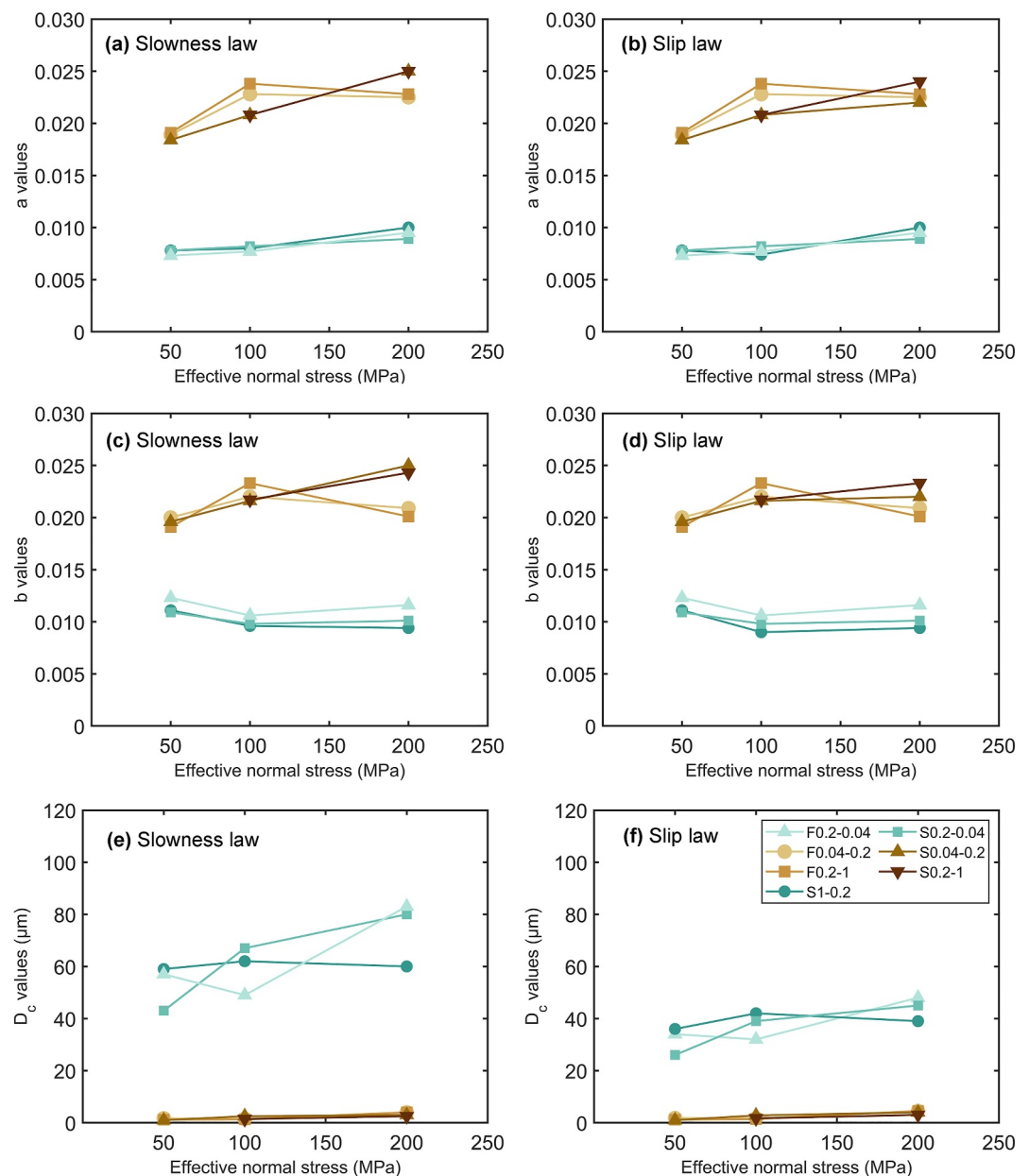


**Figure 12.** RSF parameters  $a$ ,  $b$ , and  $D_c$  at effective normal stresses of 50–200 MPa, (a)  $a$  values, calculated using the slowness evolution law, (b)  $a$  values, calculated using the slip evolution law, (c)  $b$  values, calculated using the slowness evolution law, (d)  $b$  values, calculated using the slip evolution law, (e)  $D_c$  values, calculated using the slowness evolution law, and (f)  $D_c$  values, calculated using the slip evolution law.

et al. (2012) and den Hartog & Spiers (2013, 2014). Even though the model was initially applied to explain the stability evolution with the temperature for muscovite-halite or quartz-illite gouges, it has more universal application (Boulton et al., 2014; He et al., 2016; Sawai et al., 2016). During shearing, granular flow may induce dilation. In this microphysical model, the gouge dilation induced by granular flow is countered by thermally activated compaction controlled by pressure solution—and thus this competition between the gouge dilation and compaction primarily controls the evolution of frictional stability at different temperatures. At the same effective stress but lower temperatures (e.g.,  $T = 100^\circ\text{C}$ – $200^\circ\text{C}$  in this study), the pressure solution is relatively weak and insufficient to drive the apparent compaction—and gouge dilation by particle granular flow dominates as presented in the velocity-strengthening response. At the same effective stress but higher temperatures (e.g.,  $T = 300^\circ\text{C}$ – $500^\circ\text{C}$  in this study), the glaucophane pressure solution becomes strong and dominant and thermally

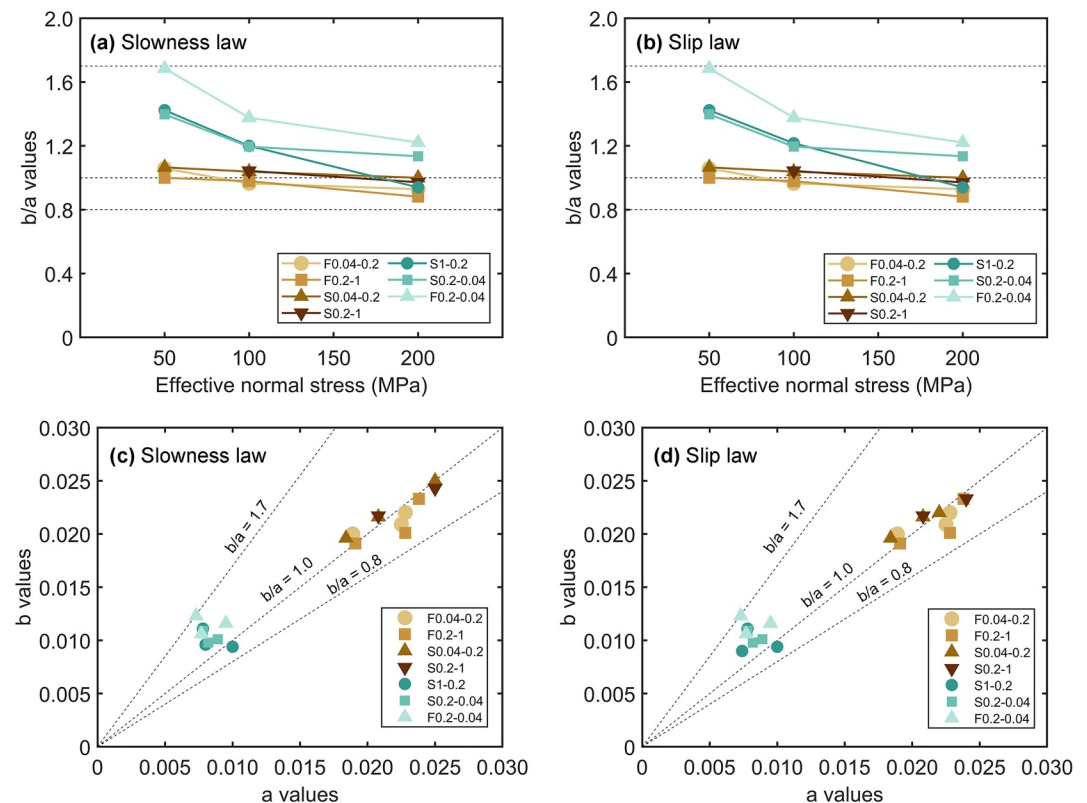


**Figure 13.** Frictional constitutive parameter  $b/a$  and the  $b$  values versus  $a$  values at effective normal stresses of 50–200 MPa (i.e., tests Gla-T300, Gla-T300-E100, and Gla-T300-E50), (a)  $b/a$  values, calculated using the slowness evolution law, (b)  $b/a$  values, calculated using the slip evolution law, (c)  $b$  values versus  $a$  values, calculated using the slowness evolution law, (d)  $b$  values versus  $a$  values, calculated using the slip evolution law.

activated compaction balances the shear-induced gouge dilation but not apparently affect the shear deformation. During an upward velocity step, increasing the shear velocity accelerates the granular dilation rate (e.g., Healy, 1963; Marone et al., 1990) and produces an elevated steady state gouge porosity at the post velocity upstep (i.e., the velocity post-step -change). In one interpretation, this increased porosity would result in a reduction in the dilation angle and the gouge frictional strength at the post shear velocity (Samuelson et al., 2009), yielding the observed velocity-weakening response. On the other hand, the increase in dilatancy rate results in an increase in shear strength via the rate of work to increase porosity (e.g., Frank, 1965), and thus velocity weakening would require an even larger reduction in the base coefficient of friction (Marone et al., 1990). Thus, in either interpretation the observed velocity-weakening response requires a decrease in the based coefficient of friction for an upward velocity step. At still higher temperatures, the pressure solution would be sufficiently strong that the gouge deformation would be dominated by thermally activated compaction and the coefficient of friction would also be enhanced in an upward velocity step, also yielding velocity-strengthening response. Consequently, mechanisms for the change in gouge frictional stability at different temperatures would result from the change in porosity during a velocity step. At temperatures in the range 100°C–300°C, mass transfer due to pressure solution for the glaucophane gouge would increase with increased temperature and contribute to the observed decrease in frictional stability ( $a-b$ ) (Figure 7). At 300°C–500°C, the frictional stability ( $a-b$ ) and the frictional constitutive parameters  $a$  and  $b$  remain essentially unaffected by temperature (Figures 7 and 8) and we postulate that pressure solution could be maintained at these temperatures but be insufficient to promote another transition from velocity-weakening to velocity-strengthening response.

At 300°C, instability of the glaucophane gouge is enhanced from both the reduction in effective normal stress and the elevation of pore fluid pressure (Figure 11). According to Equation 8, the reduction in effective normal stresses or related fluid pressurization could both result in a decrease in fault critical stiffness ( $K_{cr}$ ) and stabilize the fault, as shown in Figure 18. However, the reduction in effective stress could also affect the magnitudes of

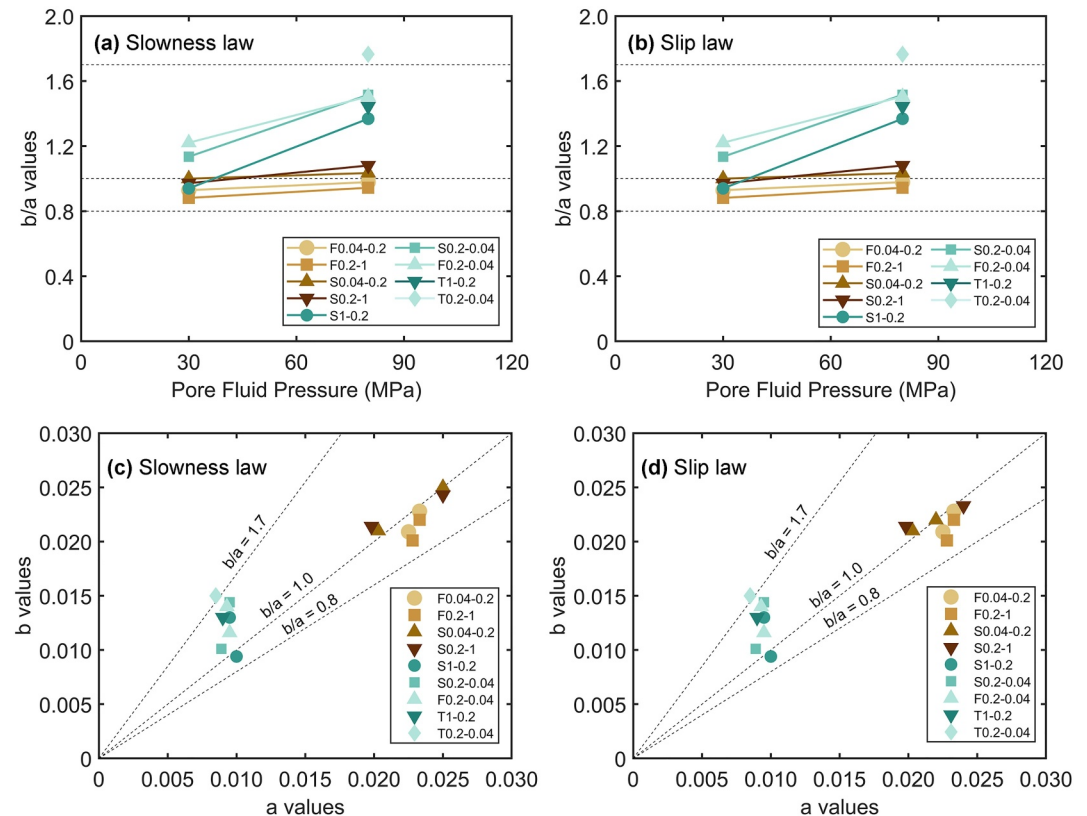


**Figure 14.** Frictional constitutive parameter  $b/a$  and the  $b$  values versus  $a$  values at pore fluid pressures of 30–80 MPa (i.e., tests Gla-T300 and Gla-T300-P80), (a)  $b/a$  values, calculated using the slowness evolution law, (b)  $b/a$  values, calculated using the slip evolution law, (c)  $b$  values versus  $a$  values, calculated using the slowness evolution law, (d)  $b$  values versus  $a$  values, calculated using the slip evolution law.

velocity dependence ( $a-b$ ) and the mechanisms of the variation of ( $a-b$ ) at different stresses can also be explained by the prior microphysical model. From the model, decreasing the effective normal stress or elevating the pore fluid pressure at the same high temperature would be equivalent to decreasing the thermally activated gouge compaction by pressure solution. Upon application of a velocity up-step, the steady state gouge porosity would be higher at the post-shear velocity and lower effective stresses. Therefore, the dilation angle and fault frictional strength would be lower and contribute to the enhanced velocity-weakening behavior. From the microstructures of the deformed gouges (Figures 16 and 17), the presence of moderately localized shear zones gradually increases with the reduction in effective normal stress and these can also reflect an increase in gouge porosity at lower effective stresses. The relative proportions of SSZ might be an indicator of the dominance of pressure solution that are more evident at reduced effective stresses but not elevated temperatures.

### 4.3. Implications for Diverse Fault Slips Modes

Abundant intermediate-depth (moderate-sized) earthquakes within cold subducting slabs and slow earthquakes with large ruptures have both been observed as associated with the fluid overpressures induced by the released water from oceanic basalt crust within blueschist layers (Hacker et al., 2003; Jung et al., 2004; van; Keken et al., 2012; Kim et al., 2013, 2015; Nishikawa et al., 2023; Schmidt & Poli, 1998). We perform laboratory shear experiments on the pure glaucophane gouge specifically at confining pressures of 55–130 MPa, pore fluid pressures of 30–80 MPa and temperatures of 100°C–500°C, to represent this subducted fluid overpressure environment—and to understand the frictional and stability properties of glaucophane gouge. The glaucophane shear experiments, together with the microstructural observations, indicate a transition from velocity-strengthening (aseismic) to velocity-weakening (potentially) responses at a temperature of 300°C. Both decreasing the effective stress or similarly elevating the pore fluid pressures, potentially as a result of pore collapse within basalt in subduction zones (Figure 1) (Nishikawa et al., 2023), specifically at 300°C may trigger



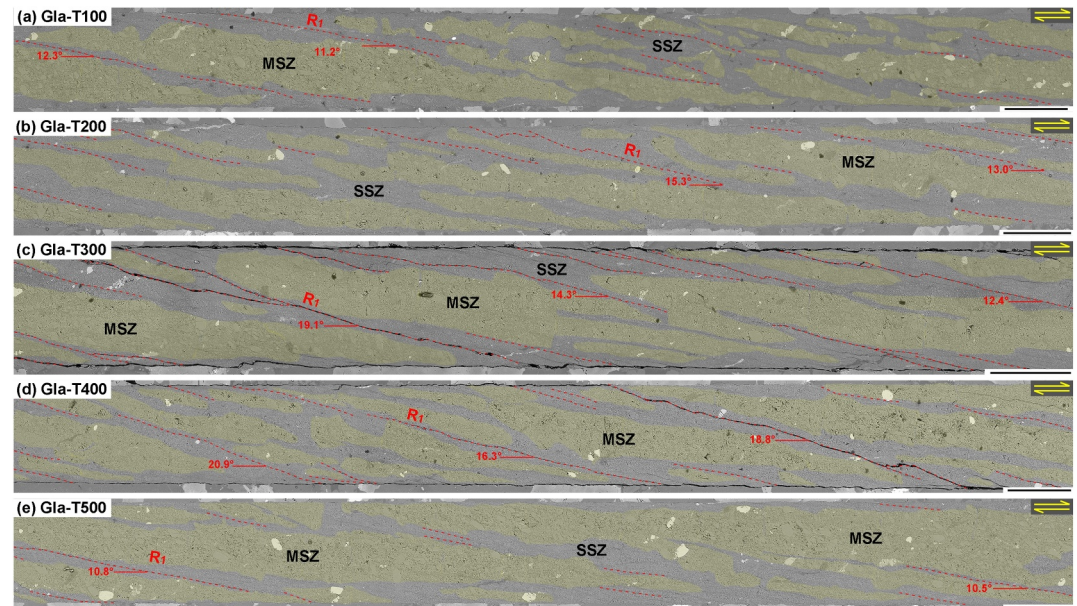


**Figure 15.** Microstructures (backscattered images) of deformed gouges for tests (a) Gla-T100, (b) Gla-T200, (c) Gla-T300, (d) Gla-T400, and (e) Gla-T500. The yellow covered areas represent the moderately localized shear zones (MSZ) with larger particles and the other regions (uncovered areas) are the strongly localized shear zones (SSZ) with very fine particles. The red dashed lines indicate the localized shear deformations and primarily  $R_1$  shears. Scales bars, 500  $\mu\text{m}$ .

fault instability. Results obtained from these experiments show that the glaucophane gouges exhibit velocity-strengthening and weak to moderate velocity-weakening behaviors, depending on the temperatures, effective normal stresses, and pore fluid pressures. At relatively lower effective normal stresses, the gouges exhibit relatively minor to moderate velocity-weakening behaviors and the critical stiffnesses also approach or are lower than fault stiffness, indicative of the potential for slow-slip events. Thus, the experimental results presented are compatible with observations of slow-slip events, episodic tremor and slip or (moderate-sized earthquakes), depending on the boundary conditions and sliding velocities.

From many previous studies, fault instabilities are shown to be closely related to ambient in situ temperatures and pressures (Moore & Lockner, 2008; den Hartog & Spiers, 2013; Faulkner et al., 2018; Tian & He, 2019) specific to a particular plate subduction habit. An increase in temperature or a reduction in effective stress could each activate the velocity strengthening-weakening transition for crustal faults (Blanpied et al., 1995; King &

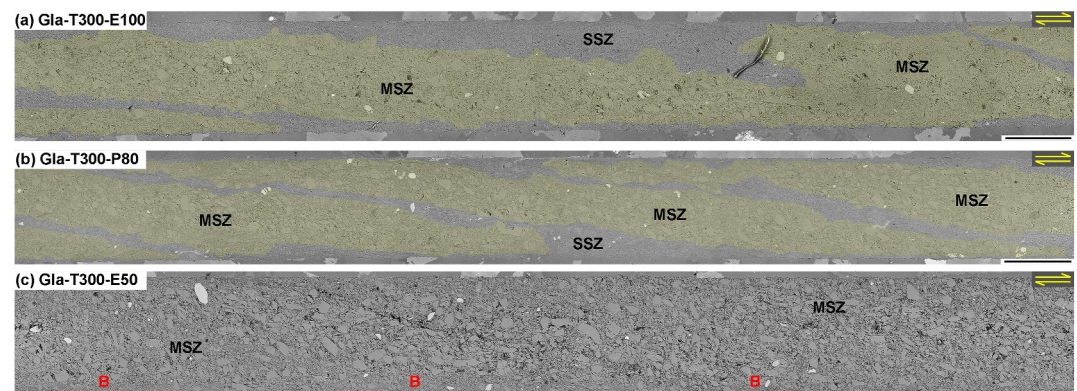


**Figure 16.** Microstructures (backscattered images) of the deformed glaucophane gouge for tests (a) Gla-T300-E100, (b) Gla-T300-P80, and (c) Gla-T300-E50. As most areas in (c) are moderately localized shear zones (MSZ) and thus they are not denoted as yellow areas. The red dashed lines indicate the localized shear deformations and primarily B shears. Scales bars, 500  $\mu\text{m}$ .

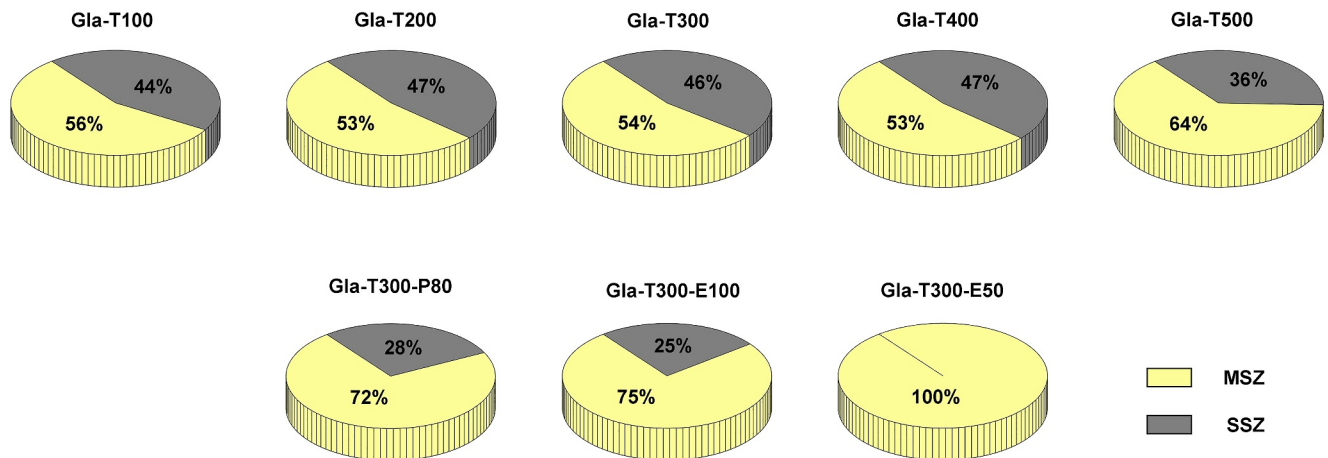


**Figure 17.** Comparisons of the proportions of the moderately localized shear zone (MSZ) to the strongly localized shear zone (SSZ) in each shear test.

Marone, 2012; Niemeijer & Colletini, 2014; Rice, 1992). Based on our experimental results, which indicate that inherent fault aseismic sliding occurs at lower temperatures of 100°C–200°C, weak velocity-weakening behavior is inferred to result in potentially seismic slip in blueschist facies at temperatures of 300°C–500°C and for high stresses—exactly the conditions presumed for a cold slab. At lower effective normal stresses or high pore fluid pressures, the growing velocity-weakening response would be capable of inducing much stronger seismic slip. Hence, intermediate-depth intraplate earthquakes associated with the instability of glaucophane gouge could also be promoted by the reduction in confined effective stress or fluid pressurization at the blueschist facies temperatures.

Finally, we note that our experiments have several shortcomings in recreating the *in-situ* pressure conditions or the gouge materials. Total stresses for blueschist facies are typically on the order of GPa—outside the limit of our apparatus. However, if highly over-pressured, then effective stresses explored within this study are potentially within an appropriate range. Additionally, the granular glaucophane gouge is also not an ideal material for conducting the shear experiments as it cannot represent the initial compaction state under pressures of GPa—unless overpressures are high and compaction state is thus reduced. Two improvements for any future studies would include experiments probing higher total stresses (e.g., Okazaki & Hirth, 2016) and the use of pre-compacted/sintered specimens in representing initial conditions.

## 5. Conclusions

We explored the effects of high temperatures and varied stress on friction-stability of glaucophane gouge as an analog to faults in blueschist facies and relevant to the diversity of fault slip styles, from slow-slip events to moderate-sized earthquakes, in cold subduction zones. Velocity-stepping experiments were performed at hydrothermal conditions and the rate- and state-friction applied to assess the friction-stability. Main conclusions are described below.

1. *Impacts of temperature:* The frictional strength of glaucophane gouge is insensitive to the variation in temperature and remains  $\sim 0.7$  at 100°C–500°C. The elevated temperature could apparently destabilize the glaucophane gouge. The glaucophane gouge exhibits moderate to strong velocity-strengthening response at 100°C–200°C, but weak velocity-weakening response at 300°C–500°C. This velocity-weakening is accompanied by denser localized shears in microstructures.
2. *Impacts of effective stress:* The frictional strength of the glaucophane gouge decreases slightly with an increase in effective normal stress. Frictional instability increases with both decreased effective normal stresses or equivalently elevated pore fluid pressures. This enhanced instability is promoted by the increase in moderate shear zones in microstructures.
3. Gouge stability at different temperatures and effective stresses can be partially explained by micromechanical models that balance the competition between granular flow-induced dilation and thermally activated compaction by pressure solution (Niemeijer & Spiers, 2007).

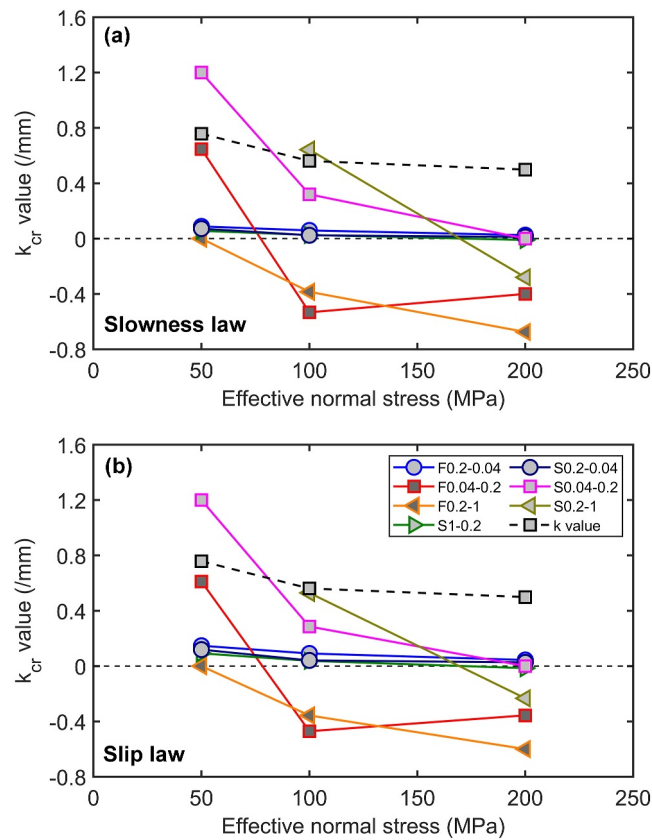


**Figure 18.** Calculated critical stiffness ( $k_{cr}$ ) values ( $k_{cr} = K_{cr}/\sigma_{neff}$ ) at normal stresses of 50–200 MPa using (a) the slowness evolution law and (b) the slip evolution law. The dashed black line indicates the calculated stiffness ( $k$ ) values. The legend shows the sequence of velocity steps with calculated values listed in Table S2 in Supporting Information S1. The calculated fault stiffness ( $k$ ) or critical stiffness ( $K_{cr}$ ) is normalized by the effective normal stress specifically to exclude the effect of the variation in effective normal stress. This normalization has no specific physical analog. The ratio of normalized critical stiffness ( $k_{cr}$ ) to normalized fault stiffness ( $k$ ) loses the effective-stress-based normalization applied to each parameter and is the stiffness-to-critical stiffness-ratio - defining the likelihood of occurrence of slow-slip events. According to Scuderi et al. (2017), and others, diverse fault slip modes are a result of controlling the ratios of  $k/k_{cr}$ . Slow-slip events frequently occur at  $k \approx k_{cr}$ . The fault stiffness  $K$  was calculated following the methods of Leeman et al. (2016) and the critical stiffness  $K_{cr}$  was calculated based on Equation 8.

4. The low values of  $(b-a)$  combined with the boundary conditions between fault stiffness and critical stiffness upon fluid pressurization support the observation of slow-slip events in glaucophane gouges at blueschist temperatures.
5. Slow-slip events and moderate-sized earthquakes are closely associated with fluid overpressures generated in the subduction processes. Our results demonstrate the enhanced instability of glaucophane gouges at lower effective stresses, which have important implications for understanding the diversity of fault slip styles from slow-slip events to moderate-sized earthquakes in cold subduction zones.

### Data Availability Statement

The friction data in this paper are available in Dryad at <https://doi.org/10.5061/dryad.2v6wvpzvr> (An et al., 2023).



**Acknowledgments**

This research is funded by the National Natural Science Foundation of China (42107163, 42320104003). DE acknowledges support from the G. Albert Shoemaker endowment. CM acknowledges support from European Research Council (ERC) advance Grant 835012 (TECTONIC), del Partenariato Esteso RETURN, finanziato dall'Unione Europea—NextGenerationEU (Piano Nazionale di Ripresa e Resilienza—PNRR, Missione 4 Componente 2, Investimento 1.3 - D.D. 1243 2/8/2022, PE0000005; Spoke VS3). We are grateful for insightful suggestions from Miki Takahashi and an anonymous reviewer that have improved the manuscript.

**References**

Abers, G. A., Nakajima, J., van Keken, P. E., Kita, S., & Hacker, B. R. (2013). Thermal-petrological controls on the location of earthquakes within subducting plates. *Earth and Planetary Science Letters*, 369–370, 178–187. <https://doi.org/10.1016/j.epsl.2013.03.022>

Ampuero, J. P., & Rubin, A. M. (2008). Earthquake nucleation on rate and state faults—Aging and slip laws. *Journal of Geophysical Research*, 113(B1), B01302. <https://doi.org/10.1029/2007JB005082>

An, M., Zhang, F., Min, K.-B., Elsworth, D., Marone, C., & He, C. (2021). The potential for low-grade metamorphism to facilitate fault instability in a geothermal reservoir. *Geophysical Research Letters*, 48(11), e2021GL093552. <https://doi.org/10.1029/2021GL093552>

An, M., Zhang, F., Yin, Z., Huang, R., Elsworth, D., & Marone, C. (2023). Data from: Friction and instability of glaucophane gouges at blueschist temperatures support abundance of intermediate-depth earthquakes [Dataset]. *Dryad*. <https://doi.org/10.5061/dryad.2v6wvwpzvr>

Audet, P., Bostock, M. G., Christensen, N. I., & Peacock, S. M. (2009). Seismic evidence for overpressured subducted oceanic crust and megathrust fault sealing. *Nature*, 457(7225), 76–78. <https://doi.org/10.1038/nature07650>

Bang, Y., Hwang, H., Kim, T., Cynn, H., Park, Y., Jung, H., et al. (2021). The stability of subducted glaucophane with the Earth's secular cooling. *Nature Communications*, 12(1), 1496. <https://doi.org/10.1038/s41467-021-21746-8>

Blanpied, M. L., Lockner, D. A., & Byerlee, J. D. (1995). Frictional slip of granite at hydrothermal conditions. *Journal of Geophysical Research*, 100(B7), 13045–13064. <https://doi.org/10.1029/95JB00862>

Boatwright, J., & Cocco, M. (1996). Frictional constraints on crustal faulting. *Journal of Geophysical Research*, 101(B6), 13895–13909. <https://doi.org/10.1029/96JB00405>

Boulton, C., Moore, D. E., Lockner, D. A., Toy, V. G., Townend, J., & Sutherland, R. (2014). Frictional properties of exhumed fault gouges in DFDP-1 cores, Alpine Fault, New Zealand. *Geophysical Research Letters*, 41(2), 356–362. <https://doi.org/10.1002/2013GL058236>

Carman, J. H., & Gilbert, M. C. (1983). Experimental studies on glaucophane stability. *American Journal of Science*, 283A, 414–437.

Colletini, C., Tesi, T., Scuderi, M. M., Carpenter, B. M., & Viti, C. (2019). Beyond Byerlee friction, weak faults and implications for slip behavior. *Earth and Planetary Science Letters*, 519, 245–263. <https://doi.org/10.1016/j.epsl.2019.05.011>

den Hartog, S. A. M., Niemeijer, A. R., & Spiers, C. J. (2012). New constraints on megathrust slip stability under subduction zone P–T conditions. *Earth and Planetary Science Letters*, 353–354, 240–252. <https://doi.org/10.1016/j.epsl.2012.08.022>

den Hartog, S. A. M., & Spiers, C. J. (2013). Influence of subduction zone conditions and gouge composition on frictional slip stability of megathrust faults. *Tectonophysics*, 600, 75–90. <https://doi.org/10.1016/j.tecto.2012.11.006>

den Hartog, S. A. M., & Spiers, C. J. (2014). A microphysical model for fault gouge friction applied to subduction megathrusts. *Journal of Geophysical Research: Solid Earth*, 119(2), 1510–1529. <https://doi.org/10.1002/2013JB010580>

Dieterich, J. H. (1979). Modeling of rock friction: 1. Experimental results and constitutive equations. *Journal of Geophysical Research*, 84(B5), 2161–2168. <https://doi.org/10.1029/JB084iB05p02161>

Fagereng, Å., & Ikari, M. J. (2020). Low-temperature frictional characteristics of chlorite-epidote-amphibole assemblages: Implications for strength and seismic style of retrograde fault zones. *Journal of Geophysical Research: Solid Earth*, 125(4), e2020JB019487. <https://doi.org/10.1029/2020JB019487>

Faulkner, D. R., Sanchez-Roa, C., Boulton, C., & den Hartog, S. A. M. (2018). Pore fluid pressure development in compacting fault gouge in theory, experiments, and nature. *Journal of Geophysical Research: Solid Earth*, 123(1), 226–241. <https://doi.org/10.1002/2017JB015130>

Frank, F. C. (1965). On dilatancy in relation to seismic sources. *Review of Geophysics*, 3(4), 485–503. <https://doi.org/10.1029/RG003i004p00485>

Frisch, W., Meschede, M., & Blakey, R. (2011). *Plate tectonics—continental drift and mountain building*. Berlin Heidelberg: Springer-Verlag.

Gao, J., & Klemd, R. (2001). Primary fluids entrapped at blueschist to eclogite transition: Evidence from the Tianshan meta-subduction complex in northwestern China. *Contributions to Mineralogy and Petrology*, 142, 1–14. <https://doi.org/10.1007/s004100100275>

Gao, X., & Wang, K. (2017). Rheological separation of the megathrust seismogenic zone and episodic tremor and slip. *Nature*, 543(7645), 416–419. <https://doi.org/10.1038/nature21389>

Giuntoli, F., Viola, G., & Sørensen, B. E. (2022). Deformation mechanisms of blueschist facies continental metasediments may offer insights into deep episodic tremor and slow slip events. *Journal of Geophysical Research: Solid Earth*, 127(10), e2022JB024265. <https://doi.org/10.1029/2022JB024265>

Gu, J. C., Rice, J. R., Ruina, A. L., & Tse, S. T. (1984). Slip motion and stability of a single degree of freedom elastic system with rate and state dependent friction. *Journal of the Mechanics and Physics of Solids*, 32(3), 167–196. [https://doi.org/10.1016/0022-5096\(84\)90007-3](https://doi.org/10.1016/0022-5096(84)90007-3)

Hacker, B. R., Peacock, S. M., Abers, G. A., & Holloway, S. D. (2003). Are intermediate-depth earthquakes in subducting slabs linked to metamorphic dehydration reactions? *Journal of Geophysical Research*, 108(B1), Subduction factory 2. <https://doi.org/10.1029/2001JB001129>

He, C., Tan, W., & Zhang, L. (2016). Comparing dry and wet friction of plagioclase: Implication to the mechanism of frictional evolution effect at hydrothermal conditions. *Journal of Geophysical Research: Solid Earth*, 121(9), 6365–6383. <https://doi.org/10.1002/2016JB012834>

He, C., Yao, W., Wang, Z., & Zhou, Y. (2006). Strength and stability of frictional sliding of gabbro gouge at elevated temperatures. *Tectonophysics*, 427(1–4), 217–229. <https://doi.org/10.1016/j.tecto.2006.05.023>

Healy, K. A. (1963). *The dependence of dilation in sand on rate of shear strain*. D. Sc. thesis. Massachusetts Institute of Technology.

Hyndman, R. D., & Peacock, S. M. (2003). Serpentinization of the forearc mantle. *Earth and Planetary Science Letters*, 212(3–4), 417–432. [https://doi.org/10.1016/S0012-821X\(03\)00263-2](https://doi.org/10.1016/S0012-821X(03)00263-2)

Jenkins, D. M., & Corona, J.-C. (2006). The role of water in the synthesis of glaucophane. *American Mineralogist*, 91(7), 1055–1068. <https://doi.org/10.2138/am.2006.2014>

Jung, H., Green, H. W., & Dobrzynetskiy, L. F. (2004). Intermediate-depth earthquake faulting by dehydration embrittlement with negative volume change. *Nature*, 428(6982), 545–549. <https://doi.org/10.1038/nature02412>

Kao, H., S.-Ju, S., Dragert, H., Rogers, G., Cassidy, J. F., & Ramachandran, K. (2005). A wide depth distribution of seismic tremors along the northern Cascadia margin. *Nature*, 436(7052), 841–844. <https://doi.org/10.1038/nature03903>

Kim, D., Katayama, I., Michibayashi, K., & Tsujimori, I. (2013). Deformation fabrics of natural blueschists and implications for seismic anisotropy in subducting oceanic crust. *Physics of the Earth and Planetary Interiors*, 222, 8–21. <https://doi.org/10.1016/j.pepi.2013.06.011>

Kim, D., Katayama, I., Wallis, S., Michibayashi, K., Miyake, A., Seto, Y., & Azuma, S. (2015). Deformation microstructures of glaucophane and lawsonite in experimentally deformed blueschists: Implications for intermediate-depth intraplate earthquakes. *Journal of Geophysical Research: Solid Earth*, 120(2), 1229–1242. <https://doi.org/10.1002/2014JB011528>

King, D., & Marone, C. (2012). Frictional properties of olivine at high temperature with applications to the strength and dynamics of the oceanic lithosphere. *Journal of Geophysical Research*, 117(B12), B12203. <https://doi.org/10.1029/2012JB009511>

Kirkpatrick, J. D., Fagereng, Å., & Shelly, D. R. (2021). Geological constraints on the mechanisms of slow earthquakes. *Nature Reviews Earth and Environment*, 2(4), 285–301. <https://doi.org/10.1038/s43017-021-00148-w>

- Kita, S., Okada, T., Nakajima, J., Matsuzawa, T., & Hasegawa, A. (2006). Existence of a seismic belt in the upper plane of the double seismic zone extending in the along-arc direction at depths of 70–100 km beneath NE Japan. *Geophysical Research Letters*, *33*(24), L24310. <https://doi.org/10.1029/2006GL028239>
- Ko, S.-C., Olgaard, D. L., & Wong, T.-F. (1997). Generation and maintenance of pore pressure excess in a dehydrating system 1. Experimental and microstructural observations. *Journal of Geophysical Research*, *102*(B1), 825–839. <https://doi.org/10.1029/96JB02485>
- Kodaira, S., Iidaka, T., Kato, A., Park, J. O., Iwasaki, T., & Kaneda, Y. (2004). High pore fluid pressure may cause silent slip in the Nankai trough. *Science*, *304*(5675), 1295–1298. <https://doi.org/10.1126/science.1096535>
- Leeman, J. R., Saffer, D. M., Scuderi, M. M., & Marone, C. (2016). Laboratory observations of slow earthquakes and the spectrum of tectonic fault slip modes. *Nature Communications*, *7*(1), 11104. <https://doi.org/10.1038/ncomms11104>
- Liu, Y., & He, C. (2020). Friction properties of hornblende and implications for slow-slip events in subduction zones. *Tectonophysics*, *796*, 228644. <https://doi.org/10.1016/j.tecto.2020.228644>
- Logan, J. M., Dengo, C. A., Higgs, N. G., & Wang, Z. Z. (1992). Fabrics of experimental fault zones: Their development and relationship to mechanical behavior. In B. Evans & T.-F. Wong (Eds.), *Fault mechanics and transport properties of rocks* (pp. 33–67). Academic Press. [https://doi.org/10.1016/S0074-6142\(08\)62814-4](https://doi.org/10.1016/S0074-6142(08)62814-4)
- Maekawa, H., Shozul, M., Ishii, T., Fryer, P., & Pearce, J. A. (1993). Blueschist metamorphism in an active subduction zone. *Nature*, *364*(6437), 520–523. <https://doi.org/10.1038/364520a0>
- Maresch, W. V. (1977). Experimental studies on glaucophane: An analysis of present knowledge. *Tectonophysics*, *43*(1–2), 109–125. [https://doi.org/10.1016/0040-1951\(77\)90008-7](https://doi.org/10.1016/0040-1951(77)90008-7)
- Marone, C. (1998). Laboratory-derived friction laws and their application to seismic faulting. *Annual Review of Earth and Planetary Sciences*, *26*(1), 643–696. <https://doi.org/10.1146/annurev.earth.26.1.643>
- Marone, C., Cocco, M., Richardson, E., & Tinti, E. (2009). The critical slip distance for seismic and aseismic fault zones of finite width. *International Geophysics*, *94*, 135–162. [https://doi.org/10.1016/S0074-6142\(08\)00006-5](https://doi.org/10.1016/S0074-6142(08)00006-5)
- Marone, C., Raleigh, C. B., & Scholz, C. H. (1990). Frictional behavior and constitutive modeling of simulated fault gouge. *Journal of Geophysical Research*, *95*(B5), 7007–7025. <https://doi.org/10.1029/JB095B05p07007>
- Mikumo, T. (1992). Dynamic fault rupture and stress recovery processes in continental crust under depth-dependent shear strength and frictional parameters. *Tectonophysics*, *211*(1–4), 201–222. [https://doi.org/10.1016/0040-1951\(92\)90059-F](https://doi.org/10.1016/0040-1951(92)90059-F)
- Miller, S. A., Collettini, C., Chiaraluce, L., Cocco, M., Barchi, M., & Kaus, B. J. P. (2004). Aftershocks driven by a high-pressure CO<sub>2</sub> source at depth. *Nature*, *427*(6976), 724–727. <https://doi.org/10.1038/nature02251>
- Moore, D. E., & Lockner, D. A. (2008). Talc friction in the temperature range 25°–400°C: Relevance for fault-zone weakening. *Tectonophysics*, *449*(1–4), 120–132. <https://doi.org/10.1016/j.tecto.2007.11.039>
- Muñoz-Montecinos, J., Angiboust, S., Garcia-Casco, A., & Raimondo, T. (2023). Shattered veins elucidate brittle creep processes in the deep slow slip and tremor region. *Tectonics*, *42*(4), e2022TC007605. <https://doi.org/10.1029/2022TC007605>
- Murrell, S. A. F., & Ismail, I. A. H. (1976). The effect of decomposition of hydrous minerals on the mechanical properties of rocks at high pressures and temperatures. *Tectonophysics*, *31*(3–4), 207–258. [https://doi.org/10.1016/0040-1951\(76\)90120-7](https://doi.org/10.1016/0040-1951(76)90120-7)
- Niemeijer, A. R., & Collettini, C. (2014). Frictional properties of a low-angle normal fault under in situ conditions: Thermally-activated velocity weakening. *Pure and Applied Geophysics*, *171*(10), 2641–2664. <https://doi.org/10.1007/s00024-013-0759-6>
- Niemeijer, A. R., & Spiers, C. J. (2007). A microphysical model for strong velocity weakening in phyllosilicate-bearing fault gouges. *Journal of Geophysical Research*, *112*(B10), B10405. <https://doi.org/10.1029/2007JB005008>
- Nishikawa, T., Ide, S., & Nishimura, T. (2023). A review on slow earthquakes in the Japan Trench. *Progress in Earth and Planetary Science*, *10*(1), 1. <https://doi.org/10.1186/s40645-022-00528-w>
- Nishiyama, N., Sumino, H., & Ujiie, K. (2020). Fluid overpressure in subduction plate boundary caused by mantle-derived fluids. *Earth and Planetary Science Letters*, *538*, 116199. <https://doi.org/10.1016/j.epsl.2020.116199>
- Obara, K., & Kato, A. (2016). Connecting slow earthquakes to huge earthquakes. *Science*, *353*(6296), 253–257. <https://doi.org/10.1126/science.aaf1512>
- Okamoto, A. S., Niemeijer, A. R., Takeshita, T., Verberne, B. A., & Spiers, C. J. (2020). Frictional properties of actinolite-chlorite gouge at hydrothermal conditions. *Tectonophysics*, *779*, 228377. <https://doi.org/10.1016/j.tecto.2020.228377>
- Okazaki, K., & Hirth, G. (2016). Dehydration of lawsonite could directly trigger earthquakes in subducting oceanic crust. *Nature*, *530*(7588), 81–84. <https://doi.org/10.1038/nature16501>
- Peacock, S. M. (1993). The importance of blueschist→eclogite dehydration reactions in subducting oceanic crust. *Geological Society of America Bulletin*, *105*(5), 684–694. [https://doi.org/10.1130/0016-7606\(1993\)105<0684:TIOBED>2.3.CO;2](https://doi.org/10.1130/0016-7606(1993)105<0684:TIOBED>2.3.CO;2)
- Peacock, S. M., & Wang, K. (1999). Seismic consequences of warm versus cool subduction metamorphism: Examples from southwest and northeast Japan. *Science*, *286*(5441), 937–939. <https://doi.org/10.1126/science.286.5441.937>
- Poli, S., & Schmidt, M. W. (1995). H<sub>2</sub>O transport and release in subduction zones: Experimental constraints on basaltic and andesitic systems. *Journal of Geophysical Research*, *100*(B11), 22299–22314. <https://doi.org/10.1029/95JB01570>
- Rathbun, A. P., & Marone, C. (2013). Symmetry and the critical slip distance in rate and state friction laws. *Journal of Geophysical Research: Solid Earth*, *118*(7), 3728–3741. <https://doi.org/10.1002/jgrb.50224>
- Reinen, L. A., & Weeks, J. D. (1993). Determination of rock friction constitutive parameters using an iterative leastsquares inversion method. *Journal of Geophysical Research*, *98*(15), 93715–93950. <https://doi.org/10.1029/93JB00780>
- Rice, J. R. (1992). Fault stress states, pore pressure distributions, and the weakness of the San Andreas fault. *International Geophysics Series*, *51*, 475–503. [https://doi.org/10.1016/S0074-6142\(08\)62835-1](https://doi.org/10.1016/S0074-6142(08)62835-1)
- Rice, J. R., & Ruina, A. L. (1983). Stability of steady frictional slipping. *Journal of Applied Mechanics*, *50*(2), 343–349. <https://doi.org/10.1115/1.3167042>
- Ruina, A. (1983). Slip instability and state variable friction laws. *Journal of Geophysical Research*, *88*(B12), 10359–10370. <https://doi.org/10.1029/JB088iB12p10359>
- Saffer, D. M., & Tobin, H. J. (2011). Hydrogeology and mechanics of subduction zone forearcs: Fluid flow and pore pressure. *Annual Review of Earth and Planetary Sciences*, *39*(1), 157–186. <https://doi.org/10.1146/annurev-earth-040610-133408>
- Saffer, D. M., & Wallace, L. M. (2015). The frictional, hydrologic, metamorphic and thermal habitat of shallow slow earthquakes. *Nature Geoscience*, *8*, 594–600. <https://doi.org/10.1038/ngeo2490>
- Samuelson, J., Elsworth, D., & Marone, C. (2009). Shear-induced dilatancy of fluid-saturated faults: Experiment and theory. *Journal of Geophysical Research*, *114*(B12), B12404. <https://doi.org/10.1029/2008JB006273>
- Sawai, M., Niemeijer, A. R., Plümper, O., Hirose, T., & Spiers, C. J. (2016). Nucleation of frictional instability caused by fluid pressurization in subducted blueschist. *Geophysical Research Letters*, *43*(6), 2543–2551. <https://doi.org/10.1002/2015GL067569>



- Schmidt, M. W., & Poli, S. (1994). The stability of lawsonite and zoisite at high pressures: Experiments in CASH to 92 kbar and implications for the presence of hydrous phases in subducted lithosphere. *Earth and Planetary Science Letters*, *124*(1–4), 105–118. [https://doi.org/10.1016/0012-821X\(94\)00080-8](https://doi.org/10.1016/0012-821X(94)00080-8)
- Schmidt, M. W., & Poli, S. (1998). Experimentally based water budgets for dehydrating slabs and consequences for arc magma generation. *Earth and Planetary Science Letters*, *163*(1–4), 361–379. [https://doi.org/10.1016/S0012-821X\(98\)00142-3](https://doi.org/10.1016/S0012-821X(98)00142-3)
- Scuderi, M. M., & Collettini, C. (2016). The role of fluid pressure in induced vs. triggered seismicity: Insights from rock deformation experiments on carbonates. *Scientific Reports*, *6*(1), 24852. <https://doi.org/10.1038/srep24852>
- Scuderi, M. M., Collettini, C., Viti, C., Tinti, E., & Marone, C. (2017). Evolution of shear fabric in granular fault gouge from stable sliding to stick slip and implications for fault slip mode. *Geology*, *45*(8), 731–734.
- Stern, R. J. (2005). Evidence from ophiolites, blueschists, and ultrahigh-pressure metamorphic terranes that the modern episode of subduction tectonics began in Neoproterozoic time. *Geology*, *33*(7), 557–560. <https://doi.org/10.1130/G21365.1>
- Tang, J., Zhang, M., Guo, X., Geng, J., & Li, Y. (2024). Investigation of creep and transport mechanisms of CO<sub>2</sub> fracturing within natural gas hydrates. *Energy*, *300*, 131214. <https://doi.org/10.1016/j.energy.2024.131214>
- Tian, P., & He, C. (2019). Velocity weakening of simulated augite gouge at hydrothermal conditions: Implications for frictional slip of pyroxene-bearing mafic lower crust. *Journal of Geophysical Research: Solid Earth*, *124*(7), 6428–6451. <https://doi.org/10.1029/2018JB016456>
- Uchida, N., Iinuma, T., Nadeau, R. M., Bürgmann, R., & Hino, R. (2016). Periodic slow slip triggers megathrust zone earthquakes in northeastern Japan. *Science*, *351*(6272), 488–492. <https://doi.org/10.1126/science.aad3108>
- Ujiié, K., Saishu, H., Fagereng, Å., Nishiyama, N., Otsubo, M., Masuyama, H., & Kagi, H. (2018). An explanation of episodic tremor and slow slip constrained by crack-seal veins and viscous shear in subduction mélange. *Geophysical Research Letters*, *45*(11), 5371–5379. <https://doi.org/10.1029/2018GL078374>
- van Keken, P. E., Kita, S., & Nakajima, J. (2012). Thermal structure and intermediate-depth seismicity in the Tohoku-Hokkaido subduction zones. *Solid Earth*, *3*(2), 355–364. <https://doi.org/10.5194/se-3-355-2012>
- Yokota, Y., & Koketsu, K. (2015). A very long-term transient event preceding the 2011 Tohoku earthquake. *Nature Communications*, *6*(1), 5934. <https://doi.org/10.1038/ncomms6934>
- Zhang, L., & He, C. (2016). Frictional properties of phyllosilicate-rich mylonite and conditions for the brittle-ductile transition. *Journal of Geophysical Research: Solid Earth*, *121*(4), 3017–3047. <https://doi.org/10.1002/2015JB012489>